Deep Free-Gas Accumulation Beneath the Chatham Rise, New Zealand—An AVO Study

Michael T. Macnaughtan[1] , **Ingo A. Pecher**[2] , **Lorna J. Strachan**[1] , and **Gareth J. Crutchley**[3]

[1]The School of Environment, The University of Auckland, Auckland, New Zealand, [2]Department of Physical and Natural Sciences, Texas A&M University, Corpus Christi, Corpus Christi, TX, USA, [3]GEOMAR Helmholtz Centre for Ocean Research Kiel, Kiel, Germany

Abstract Subduction zones serve as carbon recycling centers, where vast amassments of geologic carbon accrete or subduct through thermogenic gas windows over millions of years. We focus on New Zealand's Chatham Rise, a fossilized accretionary wedge remnant of the ~400 Myr-active East Gondwanan margin. We undertake an amplitude-variation-with-offset (AVO)-based seismic analysis of the abiogenic Mesozoic sedimentary sequence (MES) and overlying Sequence Y chalk interval, which span the Chatham Rise's northwestern slope. Two-term AVO attribute analysis resulted in the interpretation of distinct AVO Class III–IV reflection anomalies, which demarcate the siliciclastic MES from overlying Sequence Y chalks. Unified through their strong negative intercept amplitudes, Class III anomalies increase in absolute amplitude with angle, while Class IV anomalies decrease in absolute amplitude with angle of incidence. Simultaneous AVO inversion of seismic data highlighted the presence of P-impedance anomalies, which directly underlie the regionally occurring Sequence Y chalk interval. Class III anomalies are modeled and interpreted as the result of a previously undefined coarse-grained lithofacies, bearing low saturations (2%–10%) of free gas. Co-occurring ClassIV AVO anomalies are modeled to provide evidence for a fine-grained upper MES, bearing similarly low saturations of free-gas in pore space. We speculate on the gas' origin, which could be from the Hikurangi subduction margin, in situ ancient microbial activity, or a new undetermined source related to the ancient East Gondwanan subduction margin and accretionary wedge.

Plain Language Summary Active subduction zones (aka subduction margins) are globally occurring zones of geologic interest, defined by the subduction of one tectonic plate under another. Subduction margins host vast amassments of geologically bound carbon, which eventually subducts or accretes to the overriding plate. Carbon amassment and subsequent gaseous carbon-escape (e.g., methane escape) from subduction zones into the Earth's exosphere necessitate an understanding of the dominant sources of gas generation within a subduction zone. Here, we present a seismic reflection-based study of the northwestern Chatham Rise, which is a fossil remnant of the ancient East Gondwanan subduction zone. We provide seismic evidence for a previously undetected deep accumulation of carbon-bearing free gas over a large area ~50 km east of the active Hikurangi subduction margin. This gas appears trapped beneath a known sealing sediment layer consisting of chalk and mudstone, which is being subducted further to the west. We speculate on the locus of these gases and how they may be related to ancient East Gondwanan subduction or active Hikurangi subduction processes.

1. Introduction

Globally distributed sedimentary basins are estimated to have collectively amassed 10^{16} t of organic carbon within their strata (Kroeger et al., 2011). Through microbial, tectonic, and various thermal processes, a small fraction of this broadly accumulated carbon remobilizes as fluid (e.g., CH_4 and CO_2) into smaller (ca 1,000 GtC), relatively shallow (~100–1,000 m below the sea floor [mbsf]) geologic reservoirs, which may be sensitive to exospheric degassing (Galvez & Pubellier, 2019; Hessler & Sharman, 2018; Kroeger et al., 2011; Wallmann et al., 2012).

The seismic detection of concentrated or diffuse free gas such as methane (CH_4) within a subduction zone provides evidence for methanogenesis occurring across a potentially wide range of tectonically and magmatically influenced thermal windows (Hessler & Sharman, 2018; Kroeger et al., 2015; Moore & Vrolijk, 1992; ODP Leg 110 Scientific Party, 1987). While subduction margins may be suitable for long-term (millions of years) geologic

storage of carbon-bearing gases, significant methanogenesis in subduction margins is relatively rare (Hessler & Sharman, 2018 and references within).

Methanogenesis is broadly categorized into two distinct sub-types. Shallow methanogenesis relates to the anaerobic metabolic activity of microbial communities (methanogens), which produce methane as a waste product (Rice, 1993; Schoell, 1988). Methanogen productivity peaks in ~35–45°C thermal window ~1,500 m below the seafloor (mbsl), and the rate of gas generation is dominantly controlled by the sedimentation rate and total organic carbon (TOC) availability (B. J. Katz, 2011; Rice, 1993). From several thousand meters beneath the seafloor at temperatures typically >200°C, pyrolysis in carbon-rich strata results in the thermogenic expulsion of methane and higher-order hydrocarbon gases (B. J. Katz, 2011; Stolper et al., 2014; Welte, 1965).

Subduction margins characterized by accretion (e.g., von Huene and Scholl, 1991) often concentrate and amass geologic carbon, typically within their accretionary wedges but also within a downgoing, underthrusted sedimentary sequence (Hessler & Sharman, 2018; ODP Leg 110 Scientific Party, 1987; Schoell, 1988; Suzuki et al., 2024). Dictated by the geothermal gradient and TOC availability, underthrusted downgoing strata undergo thermogenesis, which continuously supports the growth of an overlying accumulation of mobile carbon-bearing gases (Hessler & Sharman, 2018). While dominantly methane, the composition of these deeply expelled thermogenic gases may be impacted by thermal alteration from subduction-related arc volcanism and magmatic intrusions, which imprint distinct isotopic signatures in gases (Poreda et al., 1988).

The location of shallow, overlying gas accumulations will vary depending on the type of margin and its subsequent tectono-sedimentary evolution (Hessler & Sharman, 2018). Margins with thick sedimentary sequences in slope- and fore arc-basins (e.g., The modern Alaska-Aleutian and ancient Farallon-Sierra margins (Scheirer et al., 2006; Stanley et al., 2011)) will accumulate vast quantities of carbon-bearing fluids, while more vigorously uplifting, deforming and eroding margins may trap fluids to a lesser degree, and continuously seep/flare fluids over vast areas (e.g., The Hikurangi Margin, Campbell et al., 2008; Crutchley et al., 2019; Watson et al., 2020; Turco et al., 2022).

Today, the Chatham Rise sits southeast of New Zealand's North Island (Figure 1). The Chatham Rise is a ~1,500 km-long, W–E trending bathymetric high, which is the fossil accretionary wedge remnant of the Mesozoic-active East Gondwanan Margin (Figure 1; Davy et al., 2008). We focus on potential gas accumulation within the Chatham Rise northwestern slope's (CRNWS) mantling strata, which were deposited following active East Gondwanan subduction (~100–~70 Ma) (Bland et al., 2015; Davy et al., 2008).

The CRNWS southwardly borders the Pegasus Basin and active Hikurangi subduction margin (HSM), sharing a common stratigraphy with them both since ~100 Ma (Figure 1; Bland et al., 2015). It is unclear whether any gases accumulating atop the remnant accretionary wedge are associated with Mesozoic-aged East Gondwanan subduction or with previously established processes related to modern HSM activity ~50 km NW (e.g., Kroeger et al., 2015, 2019; Plaza-Faverola et al., 2012).

We utilize long-offset seismic reflection data acquired in the Pegasus Basin and CRNWS to investigate seismic amplitude-variations-with-offset (AVO) in the upper strata of the Mesozoic sedimentary sequence (MES). These amplitude variations can be indicative of several rock properties such as lithology type and pore-fluid type (gas v brine) (Chopra & Castagna, 2014). Detection of geographically isolated gases or gases within abiogenic intervals may highlight the CRNWS as worthy of investigation as a new, standalone thermogenic system with potentially ancient activity spanning into the latest Mesozoic.

1.1. Chatham Rise Geologic History and Stratigraphy

The East Gondwanan margin facilitated subduction of several oceanic plates (Phoenix, Pacific, Aluk, and Hikurangi Plates) over >300 Myr, which resulted in the accretion of a >200 km-wide, >7 km-thick accretionary wedge (Davy et al., 2008; Mortimer et al., 2019; Robertson et al., 2019; van de Lagemaat et al., 2023). Following the cessation of East Gondwanan subduction ~100 Ma, the metamorphosed Chatham Rise became a ~1,500 km-long fossilized remnant of the broader accretionary wedge (Davy et al., 2008; Robertson et al., 2019).

While there is evidence for a varied style of subduction (accretionary and erosive) along the East Gondwanan margin's Mesozoic history, the Chatham Rise segment is thought to be dominated by frontal accretion at
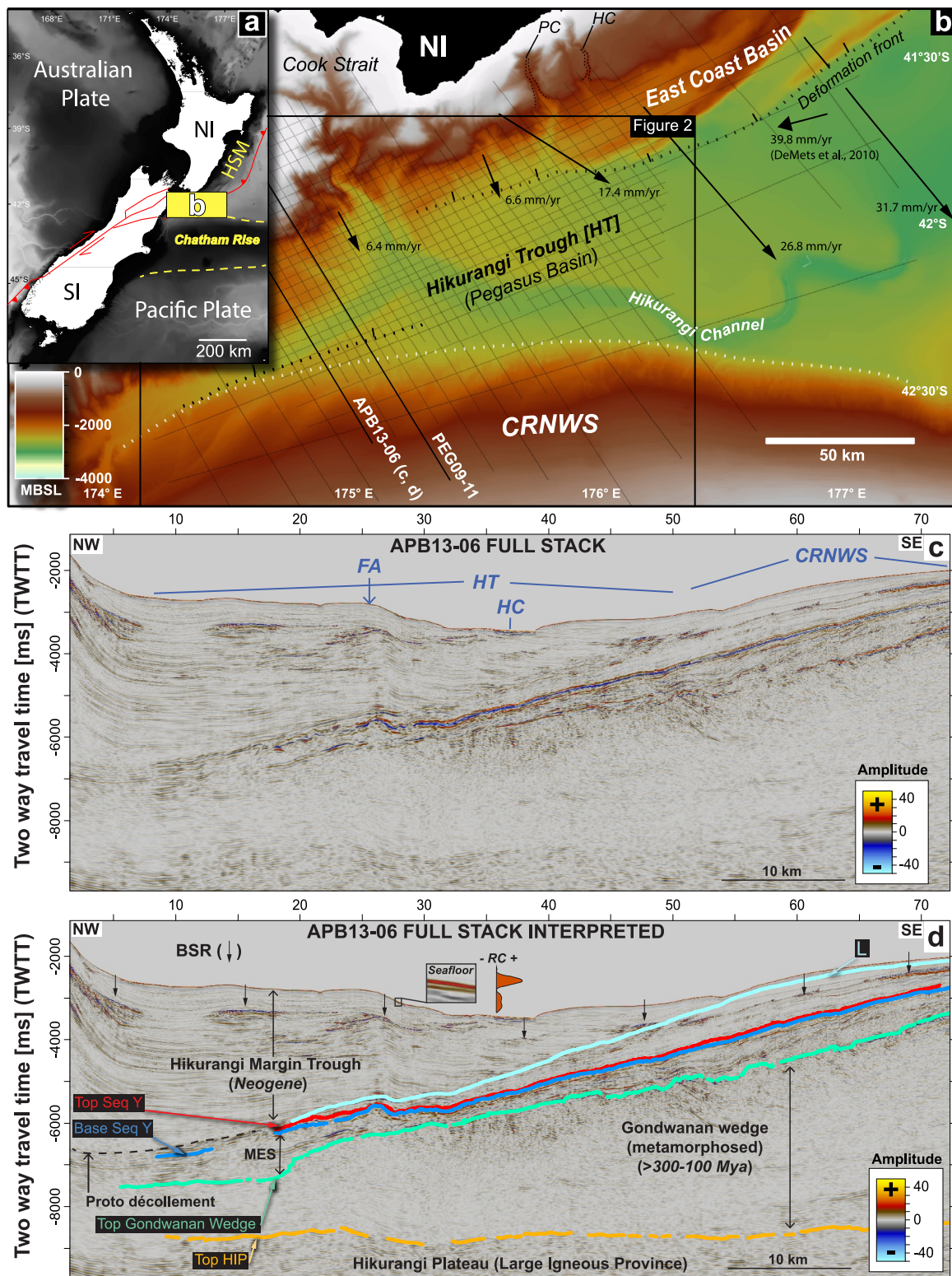
Figure 1.

~100 Ma, with no seismic evidence for underthrusting at the accretionary wedge's seaward extent (Davy et al., 2008; Ring et al., 2019; Robertson et al., 2019).

From ~110 to 100 Ma, the Hikurangi Plateau large igneous province (LIP) entered the Chatham Rise-Pegasus region and partially subducted under the East Gondwanan subduction margin (Wood & Davy, 1994). It is thought that LIP entry into the margin choked and stalled subduction (Davy, 2014; Davy et al., 2008; Mortimer et al., 2019). As LIP entry heralded East Gondwanan breakup and the separation of Zealandia by ~85 Ma, the tectonic event is marked as a major contributor to large-scale tectonic reorganization and continent formation in the southwest Pacific (Davy, 2014; Davy et al., 2008; Mortimer et al., 2019).

From ~100 to 70 Ma, the ~500–3,000 m thick MES is interpreted to have been shed from the uplifted East Gondwanan landmass following LIP emplacement (Figure 1; Davy et al., 2008). The MES is interpreted as dominantly siliciclastic, interbedded slope to basin floor turbidites, and MES mantling the Gondwanan wedge is a stratigraphic focus of our study (Figure 1; Davy et al., 2008; Kroeger et al., 2015).

Deposition of a seismically prominent nannofossil chalk interval, collectively known as Sequence Y, is thought to have been prevalent from ~70 to 32 Ma, mantling the Chatham Rise and Hikurangi Plateau (Figure 1; Barnes et al., 2010; Davy et al., 2008; Wood & Davy, 1994). The ~50 to >100 m thick, regionally occurring Sequence Y is thought to mark a period of condensed deposition where terrestrial sedimentary input was at a minimum (Carter et al., 1999).

The Neogene to Recent Chatham Rise-Pegasus Basin region is characterized as a continually infilling trench sequence, with sedimentary input modulated by (a) A continually evolving, gravity flow dominated sediment supply and (b) The development of a westerly neighboring trench slope basin system (Barnes et al., 2010; Lewis et al., 1998; McArthur et al., 2021; Figure 1). Estimates of modern oblique convergence occur at rates of 39.8 mm/year (DeMets et al., 2010; Figure 1) to 41–43 mm/year in the southern HSM (Beavan & Haines, 2001; Wallace et al., 2004). The horizontal component of subduction shows significant reduction southwestward, as slip is thought to be accommodated in upper plate strike slip faults (Wallace et al., 2012; Figure 1b).

1.2. Southern Hikurangi Subduction Margin Gas Generation

The MES is thought to host high TOC shaley intervals, which contribute to gas generation upon burial (Kroeger et al., 2015, 2019). Numerical modeling by Kroeger et al. (2015) suggests that MES-based thermogenic gas generation occurs at 12–13 km depth across the southern HSM. Thermogenic gas is proposed to migrate into the shallow subsurface, predominantly within seaward-verging thrust faults (e.g., Crutchley et al., 2019; Hillman et al., 2020; Kroeger et al., 2022; Plaza-Faverola et al., 2012), and the core of the HSM's frontal anticline (aka deformation front). Folding at the front anticline is predicted to induce cross-layer secondary permeability through the nucleation of sub-vertical fractures (Clairmont et al., 2021; Kroeger et al., 2015; Plaza-Faverola et al., 2012).

Frontal anticlines are causally linked with the development and localized enrichment of the southern HSM's gas hydrate system (Crutchley et al., 2019; Kroeger et al., 2015; Plaza-Faverola et al., 2012; Turco et al., 2020). HSM-wide evidence for gas hydrates comes through interpretation of hydrate-related bottom simulating reflections (BSRs), which mark the approximate base of gas hydrate stability (H. R. Katz, 1981; Kroeger et al., 2019; Pecher et al., 2010). Thermal modeling also highlights the significant volume of methane in the Pegasus Basin derived from in situ biogenic methanogenesis, peaking at ~1,600 mbsf (35–45°C isotherm). Microbial gas generation occurs within a thick (up to ~4 km) stratigraphic succession of rapidly deposited (~850 mm/Kyr) Pleistocene–Pliocene aged trough strata (Barnes et al., 2010; Kroeger et al., 2015; Plaza-Faverola et al., 2012; Figure 1d).

Figure 1. (a) Regional tectonic map of New Zealand. Red lines = Major faults and plate interface at the surface. Yellow rectangle = window (b). HSM, Hikurangi subduction margin; NI, North Island; SI, South Island. (b) Study area bathymetric map focused on the Hikurangi Trough and Chatham Rise northwestern slope (CRNWS). Black arrows = Horizontal component of relative slip vectors across kinematic block boundaries (see Wallace et al., 2012). Black broken line = Deformation front from Watson et al. (2020). White broken line = CRNWS base. PEG09–APB13 seismic survey line tracks overlain. Inset black polygon = Figure 2. MBSL, meters below sea level; PC, Pahaua Canyon; HC, Honeycomb Canyon. Bathymetry supplied by NIWA. (c) APB13-06 with physiographic features labeled. HC, Hikurangi Channel; HT, Hikurangi Trough. Seismic scale = Warm colors indicate increase in acoustic impedance (AI) (positive reflection coefficient). Cool colors denote a decrease in AI. (d) APB13-06 interpreted. BSR, bottom simulating reflection (black arrows); RC, reflection coefficient; Seq Y, Sequence Y; MES, Mesozoic sedimentary sequence; Top HIP, Top Hikurangi Plateau seismic horizon; L, Seismic horizon L.
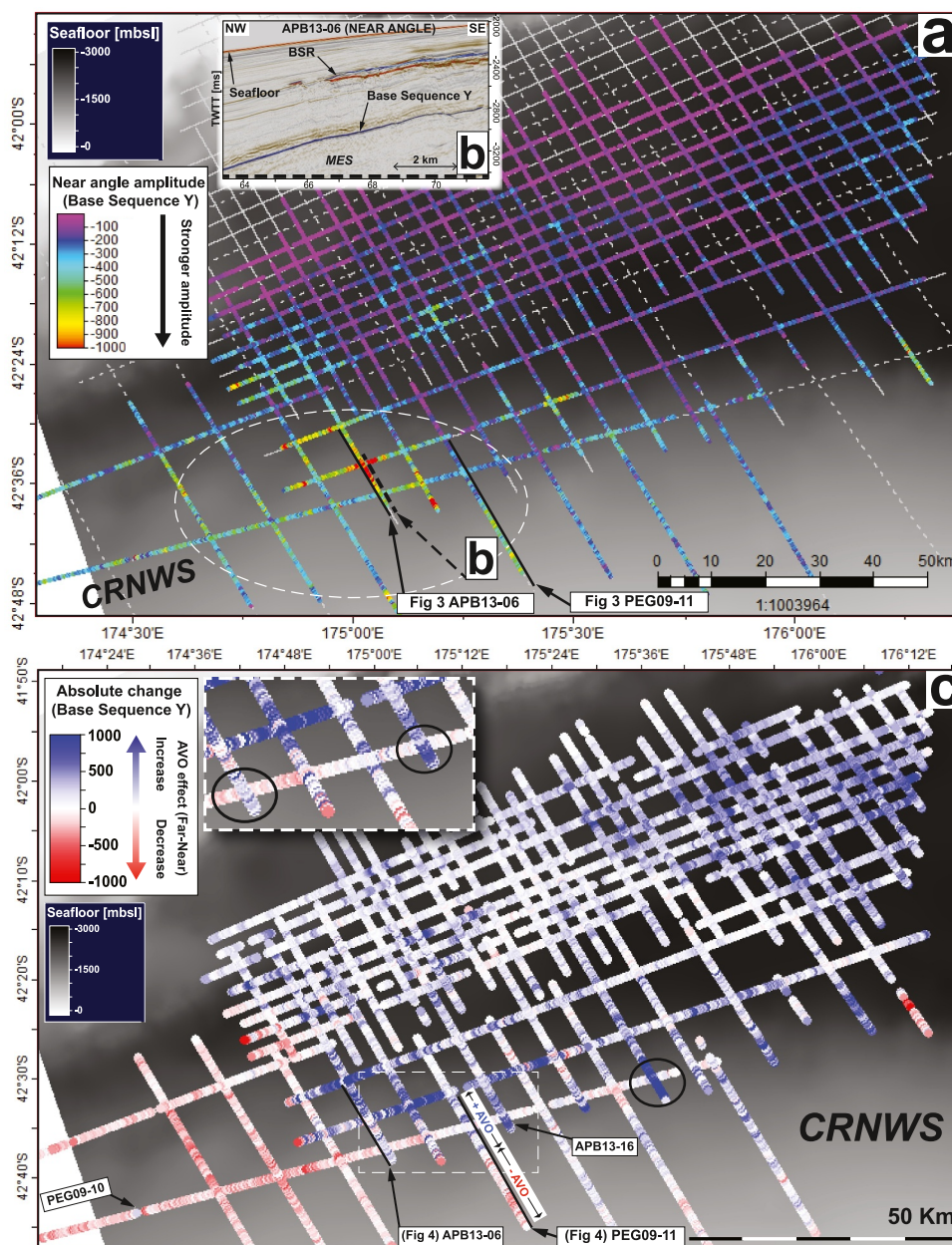
Figure 2. (a) Bathymetry overlain by extracted Base Sequence Y near-angle amplitudes (PEG09, broken white line tracks; APB13, solid white line tracks). Warming colors = stronger absolute amplitudes. Broken white line circles an area of interest. CRNWS, Chatham Rise northwestern slope. (b) Inset window of APB13-06 near-angle showing an example section of Base Sequence Y (location = broken black line). MES, Mesozoic sedimentary sequence; BSR, Bottom simulating reflection. (c) Change in absolute amplitude values of Base Sequence Y between near- and far-angle stacks. Blue-colored values indicate brightening at far angles. Red-colored values indicate dimming at far angles. A black circle highlights the APB13-28–PEG09-10 intersection with an amplitude mismatch. The white broken line box shows an inset zoomed window. Inset, two locations with mismatching amplitudes highlighted. Supporting Information S1 (Text S10 and Figure S19 in Supporting Information S1) describes these artifactual imaging issues related to Petrel™'s voxel-based attribute display. APB13-06 and PEG09-11 are highlighted and are the amplitude variation with offset (AVO) focus of this study (Figure 4).

The MES spanning the CRNWS (Figure 1d) occurs within the microbial gas thermal window; however, Kroeger et al. (2015) models MES as abiogenic, likely due to age. The underlying Gondwanan Wedge (Figure 1d) is not currently considered as a source for gas generation due to its metamorphosed metasedimentary composition (Bland et al., 2015; Kroeger et al., 2015). We note that little work has been done to explore the Chatham Rise's

Table 1
Acquisition Parameters for PEG09 and APB13

Parameter	PEG09 2D (2009)	APB13 2D (2013)
Source type	Bolt annular port airgun array	Airgun array
Volume (cu. In./L)	5,400/88.49	3,610/59.15
Streamer length (m)	10,000	8,100
Shot interval	37.5 m	37.5
No of channels	800	648
Near offset (m)	140	80
Group interval (m)	12.5	12.5
Recording length (s)	12	10.5
Sampling rate (ms)	2	2
Stack angle ranges (°)		
Near	5–18	5–18
Mid	18–32	18–32
Far	32–45	32–45
Full	Inner mute/outer mute 40	Inner mute/outer mute 40

Note. APB13 (2013) (CGG Services (Singapore) Pte. Ltd/Anadarko New Zealand Company, 2014a). PEG09 (2009) (CGG Services (Singapore) Pte. Ltd/Anadarko New Zealand Company, 2014b).

potential as a source or conduit for deeper migrating fluids. Thus, at present, the MES mantling the CRNWS (Figure 1d) is thought to be free from gas or hosting a near-undetectable volume of free gas. Our AVO investigation targets seismic reflections marking the Sequence Y to the MES interface (Figure 1d). AVO investigation assesses reflectivity at the boundary between the low permeability Sequence Y chalks (e.g., Plaza-Faverola et al., 2016) and the underlying (previously unsampled) MES, which is likely composed of siliciclastic strata (e.g., Davy et al., 2008).

2. Data and Methods

We investigate two-dimensional (2D) seismic reflection surveys covering ~30,000 km^2, supplied by the New Zealand Petroleum and Minerals online database, managed by the Ministry for Business Innovation and Employment (Figure 1). The PEG09 and APB13 surveys were acquired for exploration and as such, feature high source-energy and low dominant-source frequencies (25 and 35 Hz Turco et al., 2020).

Despite reference to offset in AVO, we use angle range-limited stacks (Table 1), which we refer to as "angle stacks." They are considered more accurate in AVO analysis due to the angle of incidence (AOI) decreasing with depth in offset-stacks (Chopra & Castagna, 2014). Full-stacks resolve structures to ~10 S two way travel time (TWTT), providing an overview of HSM stratigraphy.

Both surveys are pre-stack, time-migrated data and have undergone industry standard processing workflows, which includes 2D geometry assignment, re-sampling, noise-attenuation, seafloor-related multiple attenuation, velocity analysis and pre-stack Kirchhoff migration (CGG Services (Singapore) Pte Ltd, 2014a; Reflect Geophysical Pte Ltd, 2010). Both surveys are zero-phase data. Processing reports state the aim of preserving the AVO response in pre-stack gathers, particularly during dense velocity analysis and radon transform-based noise attenuation. All interpretations were done in time-migrated seismic sections. We interpreted time-migrated full-angle sections (e.g., Figures 1c and 1d), and limited-range angle stacks (e.g., Figure 3).

2.1. Data Preparation

Seismic data were investigated using SLB Petrel 2021™ under an academic license. The module Quantitative Interpretation™ (QI™) facilitated all AVO investigations. To use QI™ designed for three-dimensional (3D) seismic volumes (cubes), 2D seismic lines must be converted into a 3D seismic volume. Two-dimensional lines were duplicated 5–10 times with variable inline spacing using a publicly available Python script (Warnke, 2022b).
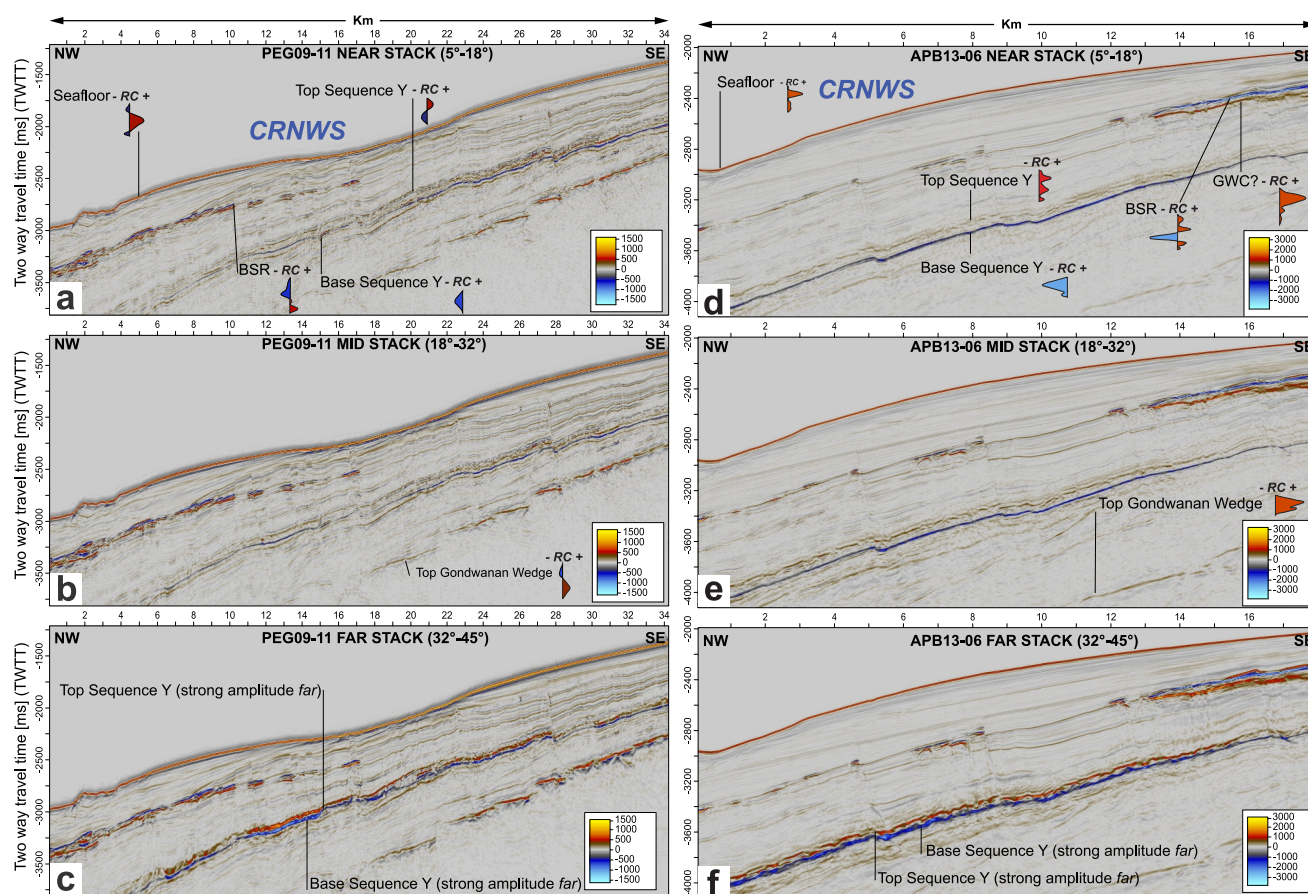
Figure 3. (a) PEG09-11 near-stack with reflections of interest labeled. Top GW, Top Gondwanan wedge; RC, Reflection coefficient. Wavelets indicating reflection polarity are overlain. (b) PEG09-11 mid-stack with interpreted gas hydrate-BSR labeled. (c) PEG09-11 far-stack with anomalous changes in absolute amplitude with angle labeled. (d) APB13-06 near-angle with labeled intervals and reflections of interest. GWC, possible gas-water-contact. (e) APB mid-stack. (f) APB far-stack with annotation. Note that the identical amplitude scales (−1,500 to 1,500) for (a)–(c) (PEG09 data) are different from the identical scales (−3,000 to 3,000) for the APB13 data (d)–(f).

Pseudo-3D volume geometry is shown within a table in Supporting Information S1. Root mean square (RMS) velocity data were converted to interval velocity data using a Dix equation-based publicly available script (Warnke, 2022a).

As shown in Figure 8a, an approximated modeled seafloor reflection appears stable in amplitude until ∼42° AOI, where it begins to increase in amplitude with angle. The seafloor reflection is therefore devoid of strong AVO effects, and should reliably appear approximately consistent across angle stacks. It is common to calibrate "true" AVO effects on the seafloor reflection/event in this way (e.g., Andreassen et al., 1997). Angle stack amplitude scales and ranges were normalized against one another according to the strength of the seafloor. Within Figure 3, consistent amplitude seafloor reflections are displayed across angle stacks for each survey (Figures 3a–3c = PEG09; Figures 3d–3f = APB13) with a common amplitude scale for each survey. The polarity of the data is SEG positive, meaning that an increase in acoustic impedance is represented by a red-infilled peak (Figure 1d).

Prior to analysis, we assessed the seafloor reflection strength of angle-stacks to determine if an adequate spherical divergence correction (V^2T) where V = velocity and T = TWTT was applied. An indicator of an appropriately applied V^2T correction is a stable seafloor amplitude that does not change systematically as a function of water depth (Figures S1 and S2 in Supporting Information S1).

2.2. Seismic Stratigraphy

Seismic horizons were interpreted upon their significance toward vertical changes in the orientation or reflective character of seismic reflections (Mitchum et al., 1977). We interpreted reflections that marked a "reflection termination boundary" as apparent unconformities or reflections that marked distinct seismic facies boundaries. Facies are described through criteria such as amplitude (absolute reflection strength), frequency (reflection cycles over TWTT) and lateral continuity (continuous-segmented) (Sangree & Widmier, 1977).

2.3. Amplitude Mapping

Using stratigraphic horizon interpretations, we extracted absolute amplitudes from near- and far angle-stacks to produce regional-scale amplitude maps. Changes in absolute amplitude with AOI are observed by subtracting far from near-angle data. Maps highlight where clear amplitude changes with angle (AVO effects) occur.

2.4. AVO Reconnaissance

AVO analysis is based on Zoeppritz (1919) equations, which describe how seismic waves behave at medium boundaries across varying AOI. Reconnaissance allows the interpreter to apply Zoeppritz approximations to pre-stack gathers or stacked data. Outputs (AVO attributes) allow the interpreter to efficiently visualize amplitudes in an AVO context (Chopra & Castagna, 2014). We use the two-term Shuey (1985) approximation, appropriate for use up to ~30° AOI. We use two attributes: the zero-offset intercept (abbreviated P) stack and the gradient (abbreviated G) stack (indicating magnitude of change in amplitude with angle). Smaller anomalous selections of anomalous reflections may be sampled from attribute stacks using a volume of interest (VOI), which then facilitates AVO crossplotting.

2.5. AVO Crossplotting

Crossplots are clear visual representations of attribute points, allowing identification of AVO trends and anomalies. Any two attributes are crossplottable; however, common "combination AVO indicators" stem from Shuey (1985) attributes. An AVO background trend (BT) is a cluster of statistically related intercept and gradient values, which is interpreted as representing brine-saturated siliciclastic rocks (Castagna & Swan, 1997). AVO background trends are commonly determinable through sampling regions that feature similarly low intercept and gradient values. Anomalously large values in either attribute (P, G) that deviate from the BT (i.e., high negative intercept, high negative gradient) are commonly indicative of anomalous lithologies or pore fluids (e.g., free gas) (Castagna & Swan, 1997).

To determine an AVO BT, we crossplot P and G values from several VOI. We add VOI to reflection intervals that appear with anomalously high reflectivity values in attribute stacks. Deviations from the P versus G BT are compared with AVO classification schemes developed by Castagna and Swan (1997), Foster et al. (2010), Rutherford and Williams (1989), and Young and LoPiccolo (2003). Interpretation of the AVO anomaly lends to geological interpretations.

2.6. Simultaneous AVO Inversion

To explain AVO anomalies in the context of rock properties, we conducted an iterative simultaneous AVO inversion (e.g., Ma, 2002) on time-migrated angle stacks using the Fatti et al. (1994) AVO approximation. To ensure event matching across angle ranges, we applied a Petrel™-based trace alignment on each angle stack using a guided non-rigid matching technique with a maximum TWTT shift of 10 ms.

Typically, borehole data are used to provide high-resolution sonic and density information, which guides AVO inversion (Chopra & Castagna, 2014). As a limitation of this inversion is the lack of borehole data, we derived these guiding values from the interval velocity model (e.g., Fohrmann & Pecher, 2012). A pseudo borehole (Text S11 and Figure S20 in Supporting Information S1) was produced for PEG09-11 and APB13-06, where interval velocity was recorded from the seafloor to with the MES. S-wave (Vs) and bulk density (ρ_b) logs were then estimated from Vp using the Castagna et al. (1985) and Gardner et al. (1974) empirical relationships, respectively. Low frequency P-, S-impedance, and density models (background trends) were then computed for each inverted line (APB13-06, PEG09-11) from respective interval velocity data-derived Vs and ρ_b logs. Prior to inversion, we extracted deterministically derived wavelets for each trace-matched angle stack range at two CRNWS pseudo

Table 2
Summary of Interpreted Seismic Stratigraphic Horizons

Horizon	Estimated age (Ma)	Horizon correlation
Horizon L	~3.5 ± 0.2	Correlates with Reflector L (Plaza-Faverola et al., 2012). "L" (Barnes, 1994a, 1994b)
Top Sequence Y	~32	Correlates with Reflector 7 (R7) (Barnes et al., 2010; Plaza-Faverola et al., 2012) Correlates to Horizon O (Barnes, 1994a)
Base Sequence Y	~70	Correlates with Sequence Y (Davy et al., 2008; Plaza-Faverola et al., 2012)
Top Gondwanan Wedge	~80	Correlates with the base of the MES unit from Davy et al. (2008) or Bst (Plaza-Faverola et al., 2012)
Top HIP	~100	Correlates with Reflector 8 (R8) (Barnes et al., 2010)

boreholes. Deterministic wavelet extraction is performed when borehole information is not available, and the method is summarized by de Macedo et al. (2016). Zero-phase wavelets were extracted from the pseudo borehole location for three angle-stacks (Figure S3 in Supporting Information S1).

2.7. AVO Modeling

Direct rock properties are used to model observed changes in amplitude with AOI within the reflection coefficient (RC) domain, thus verifying AVO observations against approximated geological reality (Ostrander, 1984). In the absence of well log data, we use Zoeppritz modeling, which is considered absolute in terms of accurate two-layer medium boundary AVO modeling. We utilize a Python script, which solves Zoeppritz (1919) equations and provides reflection coefficients with AOI.

As no southern HSM borehole exists, evaluation of Sequence Y and MES physical properties (Vp, Vs, ρ_b) is performed by examining boreholes which encountered these units. The International Ocean Drilling Programme (IODP) borehole U1520C located ~500 km NNW of the study area encountered the Sequence Y chalk interval directly overlying Hikurangi Plateau volcaniclastic strata (named Unit V) (Wallace et al., 2019). U1520C did not encounter the MES, as volcaniclastic strata are interpreted as comprising the HKB unit previously outlined by Davy et al. (2008).

Based on seismic stratigraphic interpretations of Sequence Y presented in our results, depth converted APB13-06 data (Figure S20 in Supporting Information S1) suggests the top of Sequence Y chalk is located ~200 m deeper on the CRNWS than at U1520C (~796 vs. ~991 mbsf, respectively). We compared the mean Vp of U1520C-encountered Sequence Y and its CRNWS assumed equivalent (~2,705 and ~2,762 m/s respectively). Davy et al. (2008) indicated an interval velocity for Sequence Y between 2,300 and 3,300 m/s. U1520C Vp and Vs values are therefore considered approximately representative of Sequence Y in the CRNWS, despite borehole distance from the study area. Although MES was not encountered at U1520C, Davy et al. (2008) provided an MES interval velocity range of 2,300–2,600 m/s.

AVO modeling utilizes Gassmann (1951) equations for calculating the physical effects of fluid substitution within layer media (Simm, 2007; Z. Wang, 2001). Through fluid substitution, we investigate how fluid and rock matrix driven changes in Vp, Vs, and ρ_b impact reflection coefficients (seismic amplitude) across AOI-ranges. We use a standalone application "Gassmann's Fluid Substitution v1.3" by Al-Khateb (2018) during modeling.

3. Results

3.1. Seismic Stratigraphy

Naming of the five horizons interpreted in this study follows names given by other authors when they were initially interpreted (Figure 1d; Table 2). The Top Hikurangi Plateau (Top HIP) horizon is the deepest horizon interpreted. It tracks a positive polarity reflection marking an unconformity and seismic facies change. The second deepest horizon interpreted in this study is the Top Gondwanan Wedge, which tracks a high amplitude positive polarity reflection. It is interpreted as marking an angular unconformity and seismic facies change (Figure 1).

We interpret the MES unit bound between the Top Gondwanan Wedge horizon and the Base Sequence Y horizon (Figure 1). Base Sequence Y (dark blue) is a high amplitude, continuous, negative polarity reflection compared with the seafloor, which spans the Pegasus Basin and CRNWS (Figure 1; Table 2). Overlying Base Sequence Y by ~40–100 ms TWTT, we interpret a high amplitude, continuous positive polarity reflection named Top Sequence Y (red). The latter two horizons form the bounds of the seismic unit Sequence Y (Figure 1d).

We observe low amplitude reflections overlying Sequence Y to discontinuously onlap Top Sequence Y, thus Top Sequence Y is interpreted as a regional unconformity (onlap observable in Figure 3a, line km 22–28). The stratigraphically youngest horizon interpreted in the study is labeled Horizon L (light blue) (Figure 1). Horizon L tracks a distinct angular unconformity across the CRNWS and Pegasus Basin (Figure 1). Low amplitude reflections within the Hikurangi accretionary wedge are interpreted to onlap Horizon L. Horizon L's lateral continuity toward the deformation front is unclear as continuation of Horizon L in Pegasus Basin strata could also be interpreted (e.g., Horizon L, Plaza-Faverola et al., 2012). Supporting Information S1 (Figures S4–S8 in Supporting Information S1) provides structural maps in time of each interpreted horizon.

3.2. Amplitude-Related Observations

A finding of this study is the generally high CRNWS near-angle absolute amplitude of Base Sequence Y (Figure 2a) and the change in absolute amplitude with increasing AOI (Figure 2c). We show the extracted near-angle PEG09 and APB13 absolute amplitude from Sequence Y Base horizon (Figure 2a). Supporting Information S1 shows Base Sequence Y amplitude changes in APB13 data without applying post-stack gain (Figure S9 in Supporting Information S1).

Across the Pegasus Basin, Base Sequence Y is lower in absolute amplitude (~−100 to 250 vs. seafloor, generally ~1,000 to ~1,500) with localizations of higher absolute amplitude (~−400) to the west (~174°48′E) and then northeast (~176°12′E) (Figure 2a). Examples of PEG09 and APB13 seafloor amplitudes are shown in Supporting Information S1 (Figures S1 and S2 in Supporting Information S1). There is strengthening of near-angle Base Sequence Y absolute amplitudes onto the CRNWS (Figure 2a). We highlight an area of amplitude maxima in near-angle data, where the Base Sequence Y horizon is comparable in absolute amplitude (~1,000) to the interpreted seafloor and BSR (Figure 2b).

Figure 2c shows differential amplitudes between near- and far-stacks. Positive values (cool colors) indicate a strengthening in absolute amplitude at far angles (Figure 2c). In contrast, negative values (warm colors) indicate a decrease in absolute amplitude (dimming) at far angles. These amplitude changes with angle are a proxy to AVO Class III (blue/brightening) and Class IV (red/dimming) AVO anomalies (Castagna & Swan, 1997) when near-angle amplitudes are strong (>~−600).

Across the Pegasus Basin and CRNWS, we broadly observe a bimodal distribution of positive and negative AVO effects. Exemplified by the three most western seismic lines, the CRNWS shows a weak negative AVO effect (dimming with angle) highlighted by pink colors, becoming positive to the east (Figure 2c). From ~175° eastward, the prevalence of low positive values (0 to ~250) in the Hikurangi Trough indicates an insignificant increase in absolute amplitude with angle (positive AVO effect).

Localities of high positive values colored dark blue (>750) indicate a stronger positive AVO effect, clear to the far-east of the data set (Figure 2c). The most distinct positive AVO effect occurs in the region of high near-angle amplitudes (broken white line encircled region in Figure 2a). These strong differential amplitudes (over ~1,000) span several APB13 lines, including APB13-06 (Figure 2b). To focus our AVO reconnaissance, we selected one seismic line from each survey (APB13 and PEG09):

1. APB13-06 was selected due to the strong amplitude of Base Sequence Y and a clear positive AVO effect.
2. PEG09-11 was selected as it closely tracks the strong positive AVO effects observed in the APB13 data. A shift in the AVO effect from positive to negative is observed along-line (Figure 2c).

Both lines cross interpreted BSRs, marking the base of gas hydrate stability (Figure 3). As hydrate-BSRs typically mark a known accumulation of free-gas underlying gas hydrate with little change in lithology, their respective AVO response may provide a proxy for likely gas accumulation in similar lithologies (e.g., Fohrmann & Pecher, 2012; X. Wang & Pan, 2017). Thus, we use BSR AVO responses to test methodology robustness.
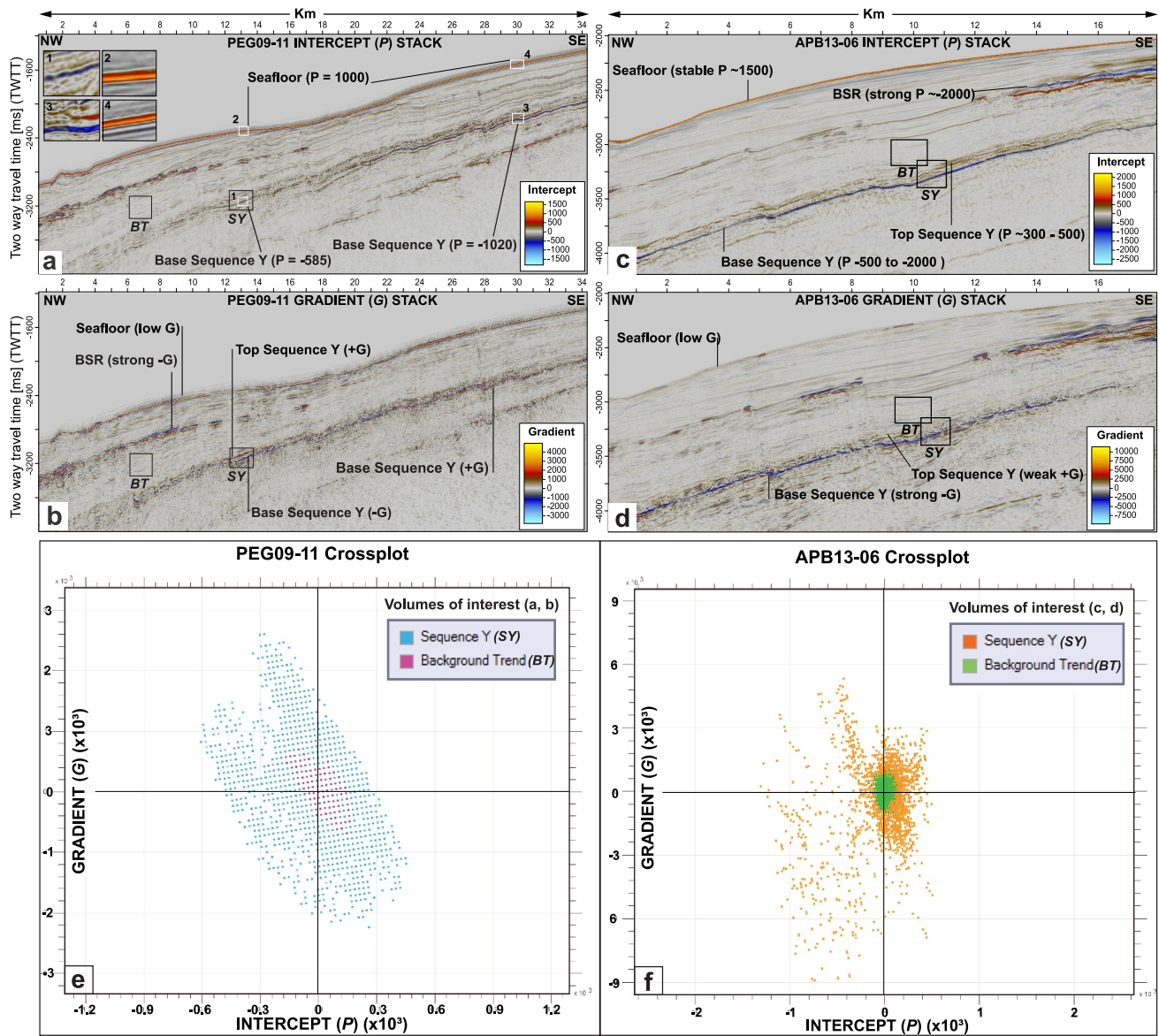
Figure 4. (a) PEG09-11 intercept stack. Black boxes labeled "BT" and "SY" are intercept volumes of interest (VOI), which are crossplotted against gradient in window e and Figure 5. BT, Background trend; SY, Sequence Y. Four inset windows labeled 1–4 show zoomed intercept values for Base Sequence Y and the seafloor. (b) PEG09-11 gradient stack BT and SY VOI are crossplotted against intercept in window (e) and Figure 5. Reflections of interest are labeled. (c) APB13-06 intercept stack with annotation. BT and SY VOI marked by black boxes sample intercept and are crossplotted against gradient in window (f) and Figure 6. (d) APB13-06 gradient stack with annotation. (e) PEG09-11 intercept versus gradient crossplot (note P and G scales are not equal). Pink values are from the BT VOI. Blue values are from the SY VOI. (f) APB13-06 intercept versus gradient crossplot. (Note P and G scales are not equal). Green points are from the BT VOI. Orange points are from the SY VOI.

In Figure 2c, inconsistent amplitude responses are observed at several seismic line intersections. Numerous mismatched amplitude responses occur at the intersection of PEG09-10 and APB13 lines, 2 of which are highlighted by an inset window in Figure 2c. These inconsistences are an artifactual response of the amplitude display method. The density of Petrel™'s voxels is difficult to image at large scales, such that small lateral changes in amplitude become unresolvable. Within the supplemental information (Text S10, Figure S19 in Supporting Information S1), we give several examples of these display artifacts and how they misrepresent numerous line intersections.

We provide several RMS amplitude-based maps in Supporting Information S1, which concern reflections bounding Base Sequence Y. Further, we provide Top Sequence Y RMS amplitude maps (Figure S10 in Supporting Information S1) in Supporting Information S1 for reference. Supporting Information S1 that shows the

RMS amplitude across the thickness of MES in full-, near-, and far-angle data (Figures S11 and S12 in Supporting Information S1).

3.3. AVO Reconnaissance

Figure 3 shows labeled reflections of interest and their reflection polarity. From visual assessment alone, trivial changes in amplitude are obvious between near- and mid-angles; however, far-angle data show some significant changes in absolute amplitude (Figures 3c and 3f).

3.3.1. Attributes

We used near- (5°–18°) and mid-angle (18°–32°) stacks to compute intercept and gradient stacks (Figure 4). The intercept attribute stack depends only on the P-impedance contrasts of the rocks; thus, intercept amplitudes should represent acoustic information and not contain any reflective anomalies tied to Poisson's ratio and far angle gas effects (Chopra & Castagna, 2014). The gradient attribute stack indicates the steepness of the line of best fit (Figures 4b and 4g).

3.3.1.1. PEG09-11 Intercept and Gradient

We observe the Base Sequence Y horizon with a strong negative intercept amplitude in the SE, becoming more positive (decreasing in absolute intercept amplitude) toward the NW (Figure 4a). Absolute intercept values here are comparable to the seafloor (∼−800 to −1,020). To the SE, Base Sequence Y intercept amplitudes reach ∼−600 (Figure 4a). The Top Sequence Y reflection is observed with a positive intercept, albeit varying in strength with values rarely exceeding ∼500 (Figure 4a). To the NW, the Top Sequence Y intercept amplitude is observed as low (∼100–150), comparable to overlying reflections (Figure 4a).

Toward the NW, a hydrate-BSR is interpreted with a strong absolute intercept amplitude, comparable to the seafloor (Figure 4a). The presence of a free-gas zone results in a strong Vp reduction and thus a strong negative polarity seismic reflection (Singh et al., 1993). The strongest gradient values are observed at the BSR (>−1,000) and indicate an increase in absolute amplitude with angle.

For the Base Sequence Y reflection, we observe generally strong absolute gradient amplitudes (∼800–1,000), which vary in sign (Figure 4b). From line position 34 km in the SE to ∼14 in the NW, the Base of Sequence Y displays a positive gradient (Figure 4b). As the Base of Sequence Y is a negative polarity reflection, positive gradient values indicate a decreasing (dimming) reflection amplitude with increasing angle (Castagna et al., 1998). Contrastingly from line position ∼14 km to the NW, we observe the Base Sequence Y reflection to have a negative gradient value (blue reflection), indicating an increase in absolute amplitude with angle.

3.3.1.2. APB13-06 Intercept and Gradient

The Base Sequence Y reflection shows a high negative intercept amplitude, which is comparable in absolute amplitude to the seafloor (Figure 4c). Lower intercept amplitudes appear between line position ∼2 to ∼4 km and to the SE of the line from ∼15 km. The BSR shows high intercept amplitude, even exceeding the seafloor in absolute amplitude (>1,000).

Top Sequence Y shows a low to moderate intercept amplitude (∼300). The gradient stack is shown in Figure 4d. The Base Sequence Y horizon shows a high negative gradient amplitude. Base Sequence Y reduces in gradient southeastward to approximately background values. The BSR displays high negative gradient values. The Top Sequence Y horizon shows notably lower gradient values than the underlying Base Sequence Y (Figure 4d).

3.3.2. Intercept Versus Gradient Crossplotting

Despite covering a large depth range and varying in petrophysical characteristics, "background" rocks (indicative of siliciclastic, brine-bearing rocks in the Rutherford and Williams (1989) scheme) generally conform to a linear trend where intercept and gradient are negatively correlated (Castagna et al., 1998). We note that "unusual" lithologies (e.g., volcaniclastics and carbonates) can deviate from these trends strongly in ways similar to gasbearing siliciclastic strata (Chopra & Castagna, 2014; Rutherford & Williams, 1989). Thus, sound local a priori geological understanding should be applied when determining what are "background" AVO responses, AVO
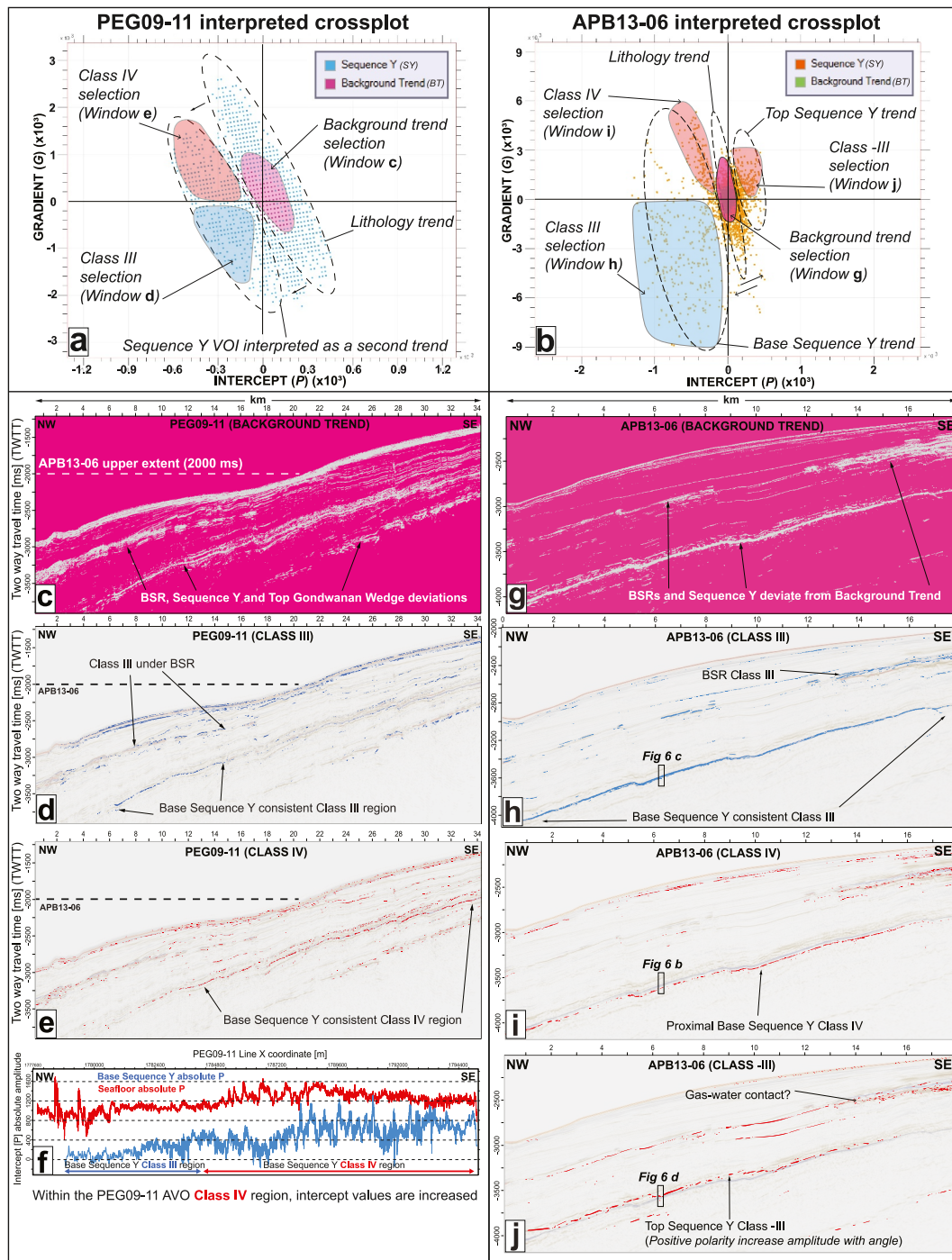
Figure 5. (a) PEG09-11 interpreted intercept versus gradient crossplot using two volumes of interest (VOI) from Figures 4a and 4b. Black broken line ellipses highlight two approximate trends. Three colored crossplot classification selections (polygons) are overlain. The spatial distribution of intercept and gradient points within each red and blue polygon (the anomalies) is depicted individually in windows (c)–(e). (b) APB13-06 interpreted intercept versus gradient crossplot using two VOIs from Figures 4c and 4d. Three crossplot trends are highlighted by black broken line ellipses. Four colored crossplot classification selections (polygons) are overlain. The spatial distribution of intercept and gradient points within each red and blue polygon (the anomalies) are depicted in windows (g)–(j). (c) The highlighted PEG09-11 background trend (BT) intercept versus gradient points are plotted onto X and Y seismic coordinates. Pink represents intercept versus gradient values located within the pink polygon in window (a). Gray represents intercept and gradient values outside the pink polygon in window (a). The black broken line represents the shallowest seafloor depth of APB13-06 (2,000 ms two way travel time (TWTT) shown in window (g)–(j)). (d) PEG09-11 intercept stack for reference. Amplitude variation with offset (AVO) Class III intercept versus gradient points are superimposed in blue. (e) PEG09-11 intercept stack with Class IV AVO intercept versus gradient anomalies superimposed in red. (f) Absolute intercept amplitudes of the seafloor (red) and Base Sequence Y (blue) plotted against PEG09-11 X-coordinates (UTM 60S coordinate

anomalies due to unusual lithologies, and AVO anomalies resulting from varying pore fluids (Castagna et al., 1998).

The black boxes labeled "BT" in Figures 4a–4d are BT VOI, which sample reflections of low intercept and gradient amplitude in PEG09-11–APB13-06 respectively. BT VOIs target reflections that are void of obvious AVO anomalies (Figures 4a–4d). These points will cluster toward the center of a crossplot, and should be representative of brine-saturated, siliciclastic strata (e.g., Castagna et al., 1998). We observe reflections bounding Sequence Y (Unit L and MES) are similarly low in intercept and gradient amplitude, conforming to approximately identical AVO background trends in the crossplot domain (Figures 4e and 4f).

The strongest deviations in intercept and gradient are observed at the BSR (Figures 4b and 4c) and Sequence Y (Figures 4a, 4c, and 4d). Inset windows labeled (1–4) within Figure 4a highlight the intercept of Base Sequence Y ranging from ∼−500 to −1,000 compared with the seafloor (∼1,000).

The black boxes labeled "SY" are ∼200 ms TWTT-thick VOI, which sample the entire Sequence Y interval and several bounding reflections within intercept and gradient stacks (Figures 4a and 4b [PEG09-11]; Figures 4b and 4c [APB13-06]). Sampled points from the VOI "SY" will highlight AVO anomalies at the Base Sequence Y reflection, and within any reflections bounding Sequence Y by ∼50 ms TWTT (Figures 4a and 4c).

It was important to use a larger sample window (VOI) to completely encompass Sequence Y, therefore allowing Sequence Y's isolation within the crossplot domain. Points sampled from the SY VOI are shown as blue and orange crossplot points for PEG09-11 and APB13-06, respectively (Figures 4e and 4f). Importantly, the Sequence Y VOI depicts how reflections (blue and orange crossplot points) deviate away to the top right and bottom left from the BT (magenta and green points) in the crossplot (Figures 4a and 4b).

In theory, intercept and gradient values should have the same order of magnitude, yet within real data the two may differ by as much as 10 due to physical processes such as absorption (Smith & Gidlow, 1987) and presence of noise (Cambois, 1998). Noise in seismic data can cause intercept and gradient values to become statistically correlated, inducing interpretation biases (Cambois, 2000). We take the investigative method of Cambois (2000) by crossplotting near- and far-stack data against the gradient to validate the presence of a lithologic trend or observe the *P* versus *G* lithologic trend masquerading as noise. Supporting Information S1 (Figure S13 and S14 in Supporting Information S1) shows these stack versus gradient crossplots and the statistically correlated sampled BT values, suggesting that our lithologic BT is representative of lithology rather than noise.

3.3.2.1. PEG09-11

Background trend values are represented as a cluster of magenta-colored points within Figure 4e. Intercept-gradient points trend from the top left to bottom right, intersecting the origin of the crossplot. Blue points are sampled from the VOI "SY," which trends parallel to the BT, albeit with a greater range in values (Figure 4e). We interpret the BT within SY and highlight a second distinct trend to the lower left of the BT (Figure 5a). While the steepness of the secondary trend mimics the BT, it departs leftward into more negative intercepts and varying gradient values (Figure 5a).

3.3.2.2. APB13-06

Within the uninterpreted crossplot, the densely clustered green-colored intercept and gradient points represent the sampled BT, steeply intersecting the origin from the top left to bottom right crossplot quadrant (Figure 4f). Orange intercept and gradient points sampled from SY cover Sequence Y and plot over a larger range than the BT sample (Figure 4f). Interpretation of the background lithology trend is given in Figure 5b marked by a closed black broken line. To the left of the lithology trend, we interpret and highlight a broad cluster of points. Inversely, to the upper right of the lithology trend, we interpret a smaller clustering of points (Figure 5b).

projection). (g) The highlighted PEG09-11 BT intercept versus gradient points are plotted onto X and Y seismic coordinates. Pink represents intercept versus gradient values located within the pink polygon in window (b). Gray represents intercept and gradient values outside the pink polygon in window (b). (h) APB13-06 Intercept stack shown for spatial reference. AVO Class III intercept versus gradient points are superimposed in blue. (i) APB13-06 intercept stack with interpreted AVO Class IV anomalies superimposed in red. (j) APB13-06 intercept stack with interpreted AVO Class III anomalies superimposed in red. Windows (h)–(j) show inset black boxes, which we show in Figure 6.

3.3.3. AVO Anomalies

Figures 5a and 5b show two crossplots with three and four overlain colored polygons. Intercept and gradient values inside a crossplot polygon selection are projected onto seismic data, highlighting all locations that exhibit the AVO anomaly. For example, magenta-colored polygons sample the interpreted BT (Figures 5a and 5b). Points from within these magenta-colored selections are projected onto seismic lines (Figures 5c and 5g) showing the distribution of points with these intercepts and gradient values.

In Figures 5c and 5g, most reflections are represented by intercept and gradient values within the magenta-colored crossplot polygons (BT). Labeled regions of gray correlate to the BSR, Sequence Y and Top Gondwanan Wedge reflections, which depart from the background intercept and gradient trend (Figures 5c and 5g). A black broken horizontal line in Figures 5c–5e marks the vertical extent of the CRNWS imaged within APB13-06, showing how PEG09-11 extends ~10 km further southeast onto the shallower CRNWS.

Interpretation of ellipses marked by black broken lines within Figures 5a and 5b is guided by how points deviate from the BT (magenta and green points). Points that deviate to the bottom left and top left quadrants of the crossplot typically warrant interpretation as AVO anomalies under the Castagna and Swan (1997) AVO framework.

3.3.3.1. Class III

We extend a blue polygon over the crossplot location of a typical AVO "Class III" anomaly, marked by strong negative intercept and gradient values (Figures 5a and 5b; Castagna & Swan, 1997). Detection of an AVO Class III anomaly (negative RC increasing in absolute amplitude with angle) is a common indicator of the presence of gas in the underlying material. PEG09-11's Base Sequence Y Class III anomaly is localized between ~6 and ~15 km line position (Figure 5d). Moving southeastward, the Class III anomaly disappears, and we interpret this due to a change in gradient values becoming positive to the SE (Figure 4b). The interpreted BSR shows a spatial correlation to the projected Class III anomaly in seismic data (Figure 5d). A complete reconstruction of the BSR's Class III AVO response requires a much larger highlighted polygon in the crossplot to encompass exceptionally large P and G values.

The Base Sequence Y reflection is dominantly an AVO Class III anomaly across the length of APB13-06 (Figure 5h). The Class III anomaly plots almost uniquely to the Base of Sequence Y and the BSR (Figure 5k). As shown in Figure 5b crossplot, the Class III AVO anomaly extends into strongly negative gradient values (up to ~−8,500), evidenced by the large blue polygon encircling values to the bottom left of the crossplot. Hendrickson (2001) and Swan et al. (1993) describe the gradient as significantly more sensitive to noise than intercept, resulting in larger gradient values being potentially indicative of noise. Within Supporting Information S1 (Text S6 and Figure S15 in Supporting Information S1), we explored whether the strong AVO Class III at Base Sequence Y is dependent on large gradient values (>−3,000). We note that if polygon selection focuses on more densely clustered points with lower gradient values, the Base Sequence Y reflection is still identified as a clear Class III anomaly (Supporting Information S1).

3.3.3.2. Class IV

In crossplots, Class IV anomalies sit in the top left quadrant (e.g., Figures 5a and 5b). The Class IV AVO anomaly is similar to Class III in that it shares a large negative intercept; however, amplitude changes with angle (the gradient) are inverse to those of a Class III anomaly (Castagna & Swan, 1997; Castagna et al., 1998). The Class IV polygon in the PEG09-11 crossplot (Figure 5a) projects encircled points onto the seismic line in Figure 5e. We interpret the PEG09-11 Class IV anomaly as laterally continuous from ~13 km to the end of the line in the SE, suggesting that the Base Sequence Y reflection is largely represented as a Class IV anomaly (Figure 5e). We show how the Base Sequence Y intercept values increase absolutely along the line into the Class IV anomaly (Figure 5f). Additionally, the positive polarity reflection underlying the BSR is partially represented by a Class IV anomaly.

In APB13-06, a Class IV anomaly is distributed along a reflection proximal to the Base Sequence Y horizon (Figure 5i). We interpret the Base of Sequence Y reflection at its highest absolute amplitude (trough) values to be associated with a Class III anomaly (Figure 6c). Underlying the Base of Sequence Y reflection, we interpret a second reflection cycle where the Class IV anomaly occupies a trough ~50 ms TWTT-deeper than the Class III
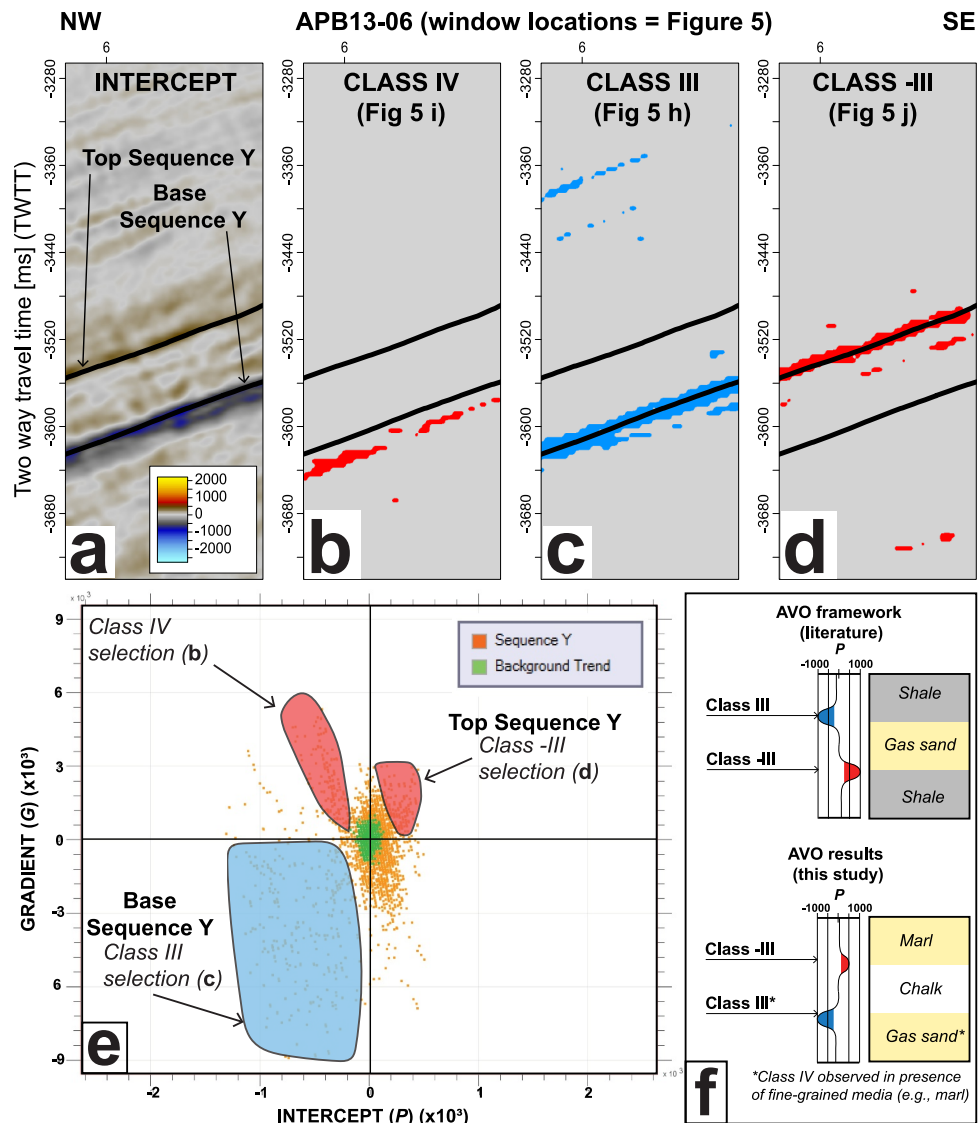
Figure 6. (a) Intercept zoomed section with Sequence Y interpretations. Windows (b), (c), (d) locations shown in Figures 5h–5j. (b) Class IV anomaly highlighted and shown in relation to horizon interpretations. (c) Class III anomaly shown in the crossplot. (d) Class III anomaly associated with the Top of Sequence Y. (e) APB13-06 crossplot with amplitude variation with offset (AVO) anomaly selections for reference. (f) Schematic of AVO gas-sand intercept responses (Foster et al., 2010) compared with our AVO anomalies and their interpreted lithologies.

anomaly (Figure 6b). Comparing windows b–c in Figure 6 illustrates this apparent localization of AVO anomalies at the Base of Sequence Y to two separate reflections.

3.3.3.3. Class III

We interpret a Class III (negative three) anomaly in APB13-06 data (Figures 6d and 6e) (Young & LoPiccolo, 2003). We isolate the anomaly and reveal its localization to the Top Sequence Y horizon (Figure 6d). As the anomaly occurs in quadrant II, it can be interpreted as a positive polarity reflection that increases in amplitude with angle. This non-standard AVO Class mirrors a Class III anomaly in the crossplot domain (Figure 6e).

3.3.4. AVO Anomaly Geological Interpretation

We summarize important AVO-based interpretations at Sequence Y, a ∼100 m thick chalk unit, thought to be bound by siliciclastic strata:

1. Top Sequence Y reflection is characterized as a Class III AVO anomaly (Figures 6d and 6f).
2. Base Sequence Y reflection is characterized by an AVO Class III or Class IV anomaly (Figures 5 and 6c).

Despite variable AVO classification within PEG09-11, Base Sequence Y is commonly characterized by a typically strong negative intercept amplitude, where the absolute amplitude ranges from half of the seafloor's amplitude (PEG09-11 $P = -585$) to larger than the seafloor amplitude (PEG09-11 $P = -1,020$) (Figures 4a and 5f).

We explored our interpretations in the context of Castagna et al. (1998)'s and Foster et al. (2010)'s investigations of gas-bearing sandstones (gas-sands) within the intercept versus gradient crossplot domain. Reflections at the top of a gas bearing sandy unit overlain by a shale (finer grained) unit will be displaced from the BT to the bottom left crossplot quadrant (Class III), due to an increase in pore fluid compressibility (e.g., gas) (Foster et al., 2010). Inversely, at the base of a gas-sand where brine replaces free-gas, a strong decrease in pore fluid compressibility results in the reflection plotting above the BT in the top right quadrant. Young and LoPiccolo (2003) label AVO anomalies that fall in this region "Type III" or "Class III" (negative 3). For congruity, we label our crossplot quadrant II (top right) anomaly as Class III.

When lithologies surrounding the gas-sand are similar, the top and base gas-sand reflections will plot equidistantly from the BT in opposing crossplot quadrants (Young & LoPiccolo, 2003). In our study, we clarify that we do not interpret a gas bearing sand unit bound by brine filled clastic or non-clastic units (Figure 6f). Despite layer arrangement, what we observe in the APB13-06 crossplot is akin in principle to these Castagna et al. (1998) and Foster et al. (2010) gas-sand interpretations, with the top and base Sequence Y reflections departing from the lithology trend into respective Class III and Class III anomalies (Figures 6e and 6f).

The occurrence of similar brine-bearing lithologies (expressed in Vp, Vs, and ρ_b) bounding Sequence Y would expectedly result in similar absolute intercept values being observed at the top and base of Sequence Y. Intercept and gradient values are representative of both lithology and pore fluid contents of both layers bounding an interface, in the case of the Class III anomaly, Sequence Y and the MES. The effect of each layer and pore fluid can be determined during AVO modeling.

We note the disparity in absolute intercept values between Class III and Class III anomalies to be a potential indicator of free-gas underlying Sequence Y. Hendrickson (2001) notes that while there is no ideal discriminator for the presence of fluids (e.g., gas) in pore space, fluid effects are primarily expressed by changes in normal-incidence P-wave response (intercept value).

Within the shallower interval of PEG09-11, we observe the Base of Sequence Y in PEG09-11 with a Class IV anomaly, shifting to Class III at ∼3,000 ms TWTT. Class IV anomaly presence is often controlled by the high porosity of the underlying gas-sand in addition to the lithology of the overlying material (Castagna et al., 1998; Foster et al., 2010). Our laterally variable AVO classifications suggest either:

- Lateral variation in the lithology or porosity of the ∼100 m thick Sequence Y chalk, resulting in varied rock properties, or;
- Lateral variation in the lithology or porosity of the underlying clastic MES unit, or;
- Variations in pore fluid type or pressure within underlying or overlying media.

3.4. Simultaneous Inversion

We inverted PEG09-11 and APB13-06 using the Fatti et al. (1994) AVO approximation. Full-length inverted sections are shown in Supporting Information S1. The inversion produces seismic sections of elastic properties, namely P-impedance (Vp * ρ_b), S-impedance (Vs * ρ_b), Vp/Vs ratios, and ρ_b. Interpretation is focused above the Top Gondwanan Wedge horizon.
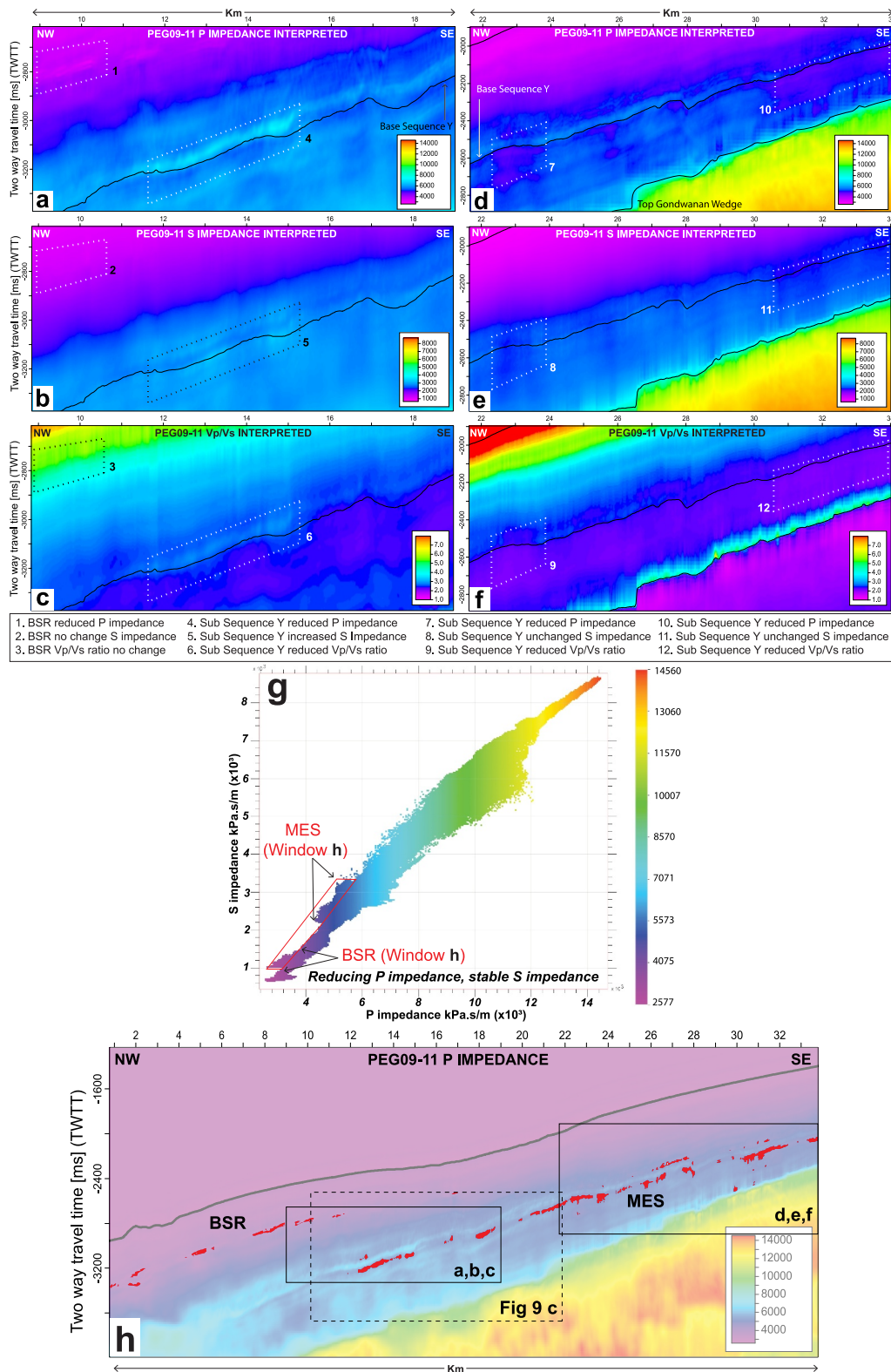
Figure 7.

3.4.1. P-Impedance

Broadly, P-impedance increases with time (warming colors with TWTT) (Figures 7a and 7d). In both data sets, Sequence Y shows higher P-impedance than bounding strata (~6,000–7,000 kPa.s/m vs. ~5,000–5,500 kPa.s/m) (Supporting Information S1; Figures 7a and 7d). In PEG09-11 (line position ~22 and 30 km), we observe two areas of low P-impedance (~4,500 kPa.s/m). The areas are approximately 1- and 5 km wide, respectively, with a thickness of ~200 ms TWTT (Figure 7b). We note a disparity in P-impedance values bounding Sequence Y at line km position ~12 km. Underlying values are slightly lower than values overlying Sequence Y, made clear by a darker blue color underlying Sequence Y (Figure 7b). Additionally, we observed a small P-impedance inversion (decrease) with depth under the BSR (Figure 7b).

3.4.2. S-Impedance

In both surveys, we observed an increase in S-impedance with TWTT (Supporting Information S1; Figures 7b and 7e). We observe the Sequence Y interval to have a lower S-impedance than bounding units (Figure 7b). In PEG09-11, Sequence Y is resolvable with lower S-impedance across the line until position ~28 km in the SE. We observe a slightly increased S-impedance in strata underlying Sequence Y compared with strata above Sequence Y (Figure 7b).

Within APB13-06, we observed Sequence Y having a lower S-impedance across the length of the line (Figures 7g and 7h). Unlike the P-impedance sections, we do not observe a resolvable change in S-impedance around the depth of the BSR (Figure 7b; Figures S18e and S18f in Supporting Information S1). Within the MES interval, we interpret a stable to slightly increasing S-impedance with increasing travel time.

3.4.3. Vp/Vs Ratios

The Vp/Vs ratio sections are shown in Figures 7c and 7f. We consider Vp/Vs ratios of Sequence Y to be accurate when compared to logging-while-drilling data obtained within the IODP U1520C borehole, which encountered Sequence Y overlying the volcaniclastic HKB unit (not MES). In our inverted data, we observe a decrease in Vp/Vs from ~2.3 to ~1.8–1.9 across the Sequence Y to MES interval (Figure 7c, Figures S18i, S18j, S18k, and S18l in Supporting Information S1). We observed the MES interval to have a laterally heterogeneous Vp/Vs structure with values typically between 1.8 and 2.0, but increasing to ~3.5 locally in areas (Figure 7f).

3.4.4. Inversion Anomalies and Crossplotting

We focus on two areas outlined by the black boxes in Figure 7h. We observed Sequence Y with higher P-impedance and lower S-impedance than surrounding strata. We observe regions of anomalously low P-impedance under Sequence Y to show nearly unchanged S-impedance (Figures 7d and 7e). Additionally, we frequently observe Vp/Vs ratios to abruptly decline beneath Sequence Y, remaining low (~2.0–1.8) within the MES (Figures 7c and 7f). The reduction in Vp/Vs and P-impedance corresponding to nearly unchanged S-impedance is anomalous and could indicate changes in either porosity or pore fluid content.

Following descriptions of Sequence Y as a widely deposited (Carter et al., 1999; Davy et al., 2008; Wood & Davy, 1994), calcite-dominated chalk unit (~95 wt% calcite, Carter et al., 1999; Wallace et al., 2019), we do not interpret any significant variation in sequence Y lithology laterally across the inverted PEG09-11. From previously modeled sub-Sequence Y Pegasus-CRNWS lithologies by Kroeger et al. (2015), we broadly assume media that directly bounds Sequence Y to likely be either quartz or clay dominated (sandstone or mudstone/shale). Calcite is likely another dominant mineral in Sequence Y-proximal rocks, owing to the gradual reduction in siliciclastic sediment supply on the subsiding and deepening Chatham Rise toward the end Cretaceous (Bland et al., 2015).

Figure 7. PEG09-11 zoomed simultaneous inversion sections. View windows (a)–(c) together. View windows (d)–(f) together. Black and white dotted boxes (labeled 1–12) correspond to key observations summarized below the sections. BSR, Bottom simulating reflection; MES, Mesozoic sedimentary sequence. (a, d) P-impedance (b, e) S-impedance. (c, f) Vp/Vs ratios. P- and S-impedance measured in kPa.s/m. (g) PEG09-11 P-impedance versus S-impedance crossplot. Values are from PEG09-11 inverted sections. The red box highlights two anomalies (deviations) from the impedance trend. Anomalies are labeled "MES" and "BSR." The anomalies of reduced P-impedance are highlighted and spatially projected in window (h). (h) PEG09-11 P-impedance section. Bright red colors are highlighted anomalies from window (g), localized to sub Sequence Y and the BSR. Black boxes are the locations of windows (a)–(f). Broken line box is the extent of window (c) in Figure 9.
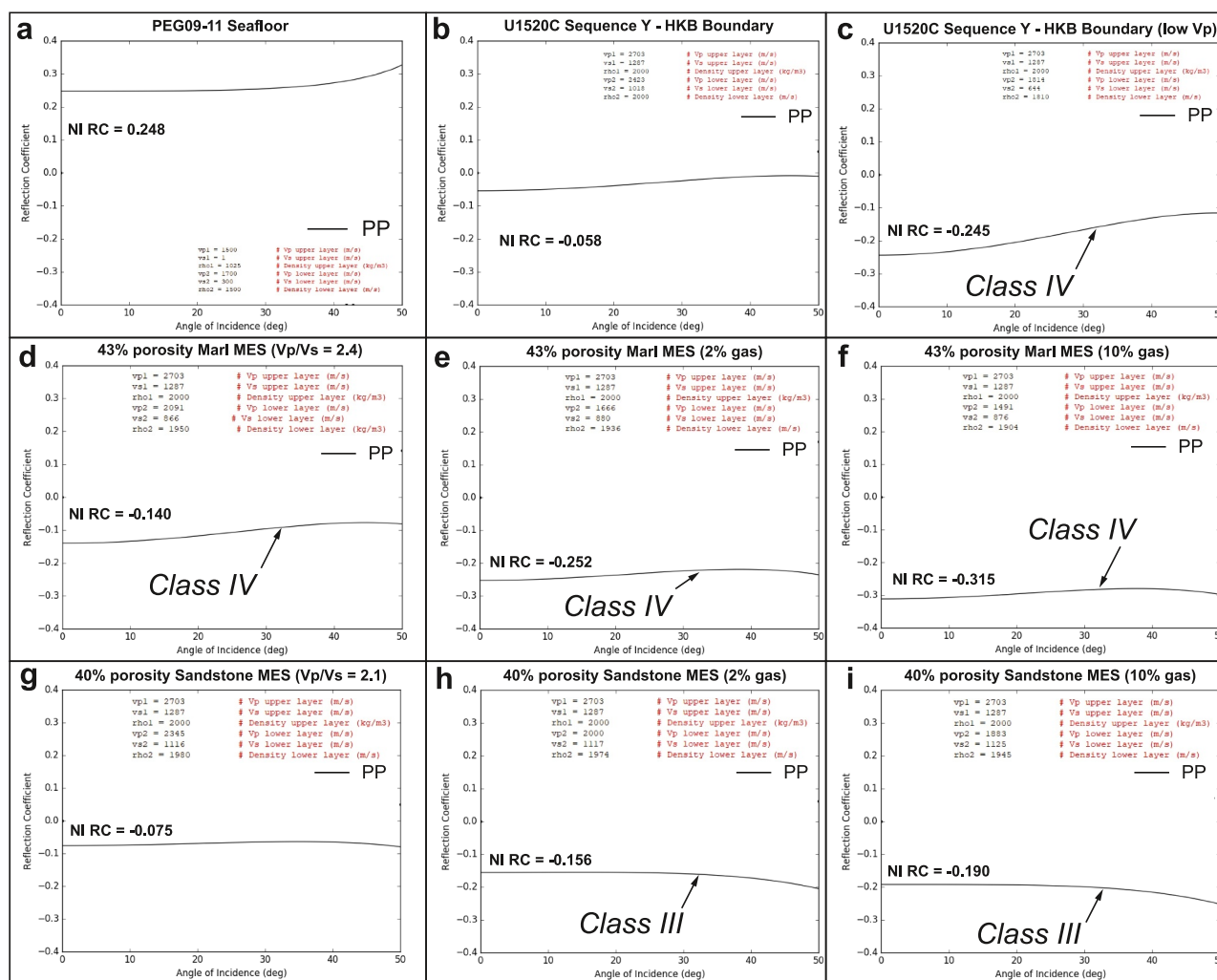
Figure 8. (a) PEG09-11 seafloor reflection coefficient (RC) with angle of incidence (AOI). NI RC, normal incidence reflection coefficient. PP, P wave to P wave reflection. (b) U1520C Base Sequence Y to Unit HKB layer boundary with representative HKB values. (c) Direct modeling of the U1520C Sequence Y to HKB boundary. Windows (d)–(i) model the Mesozoic sedimentary sequence (MES) to Sequence Y reflection on the Chatham Rise northwestern slope (CRNWS). (d) High porosity brine-saturated MES composed of marl. Marl = 50% calcite, 50% clay. Amplitude variation-with-offset (AVO) Class IV anomaly interpreted by mid angles (~32° AOI). (e) High-porosity marl MES with 2% substituted methane saturation. Class IV AVO behavior exhibited with absolute NI RC > Seafloor NI RC. (f) High-porosity marl MES with 10% substituted methane saturation. NI RC exceeds seafloor NI RC. (g) High porosity brine saturated sandstone MES. Absolute NI RC < seafloor. Sandstone = 70% quartz, 30% clay. (h) High-porosity sandstone MES with 2% substituted methane saturation. Class III AVO interpreted by mid angles (32° AOI) with absolute NI RC < seafloor. (i) High-porosity sandstone MES with 10% substituted methane saturation. Class III AVO interpreted by mid angles (32° AOI) with absolute NI RC < seafloor.

Mineralogically, the relatively higher P-impedance and lower S-impedance values of Sequence Y correspond to the absolute differences in elastic moduli (bulk and shear modulus) between calcite, clay minerals and quartz (Z. Wang, 2001). The P-impedance inversion (with stable S-impedance) underlying Sequence Y can be tracked along PEG09-11, varying in absolute strength (Figures 7a and 7d). Unlike Sequence Y, we do not assume that the underlying MES material is lithologically homogeneous in the spatial context of the CRNWS.

Therefore, mineralogical controls on inversion anomalies are considered during AVO modeling and interpretation. Avseth et al. (2016) and Castagna and Smith (1994) show how crossplotting inverted impedance and well log impedance data are useful for identifying gas-sands in particular. We crossplot P-impedance against S-impedance (Figure 7g) and P-impedance against Vp/Vs (Supporting Information S1).

Within the crossplot domain, we observed an approximately linear trend with a positive correlation between P- and S-impedance (Figure 7g). Two anomalous deviations from the trend, characterized by reduced P-impedance
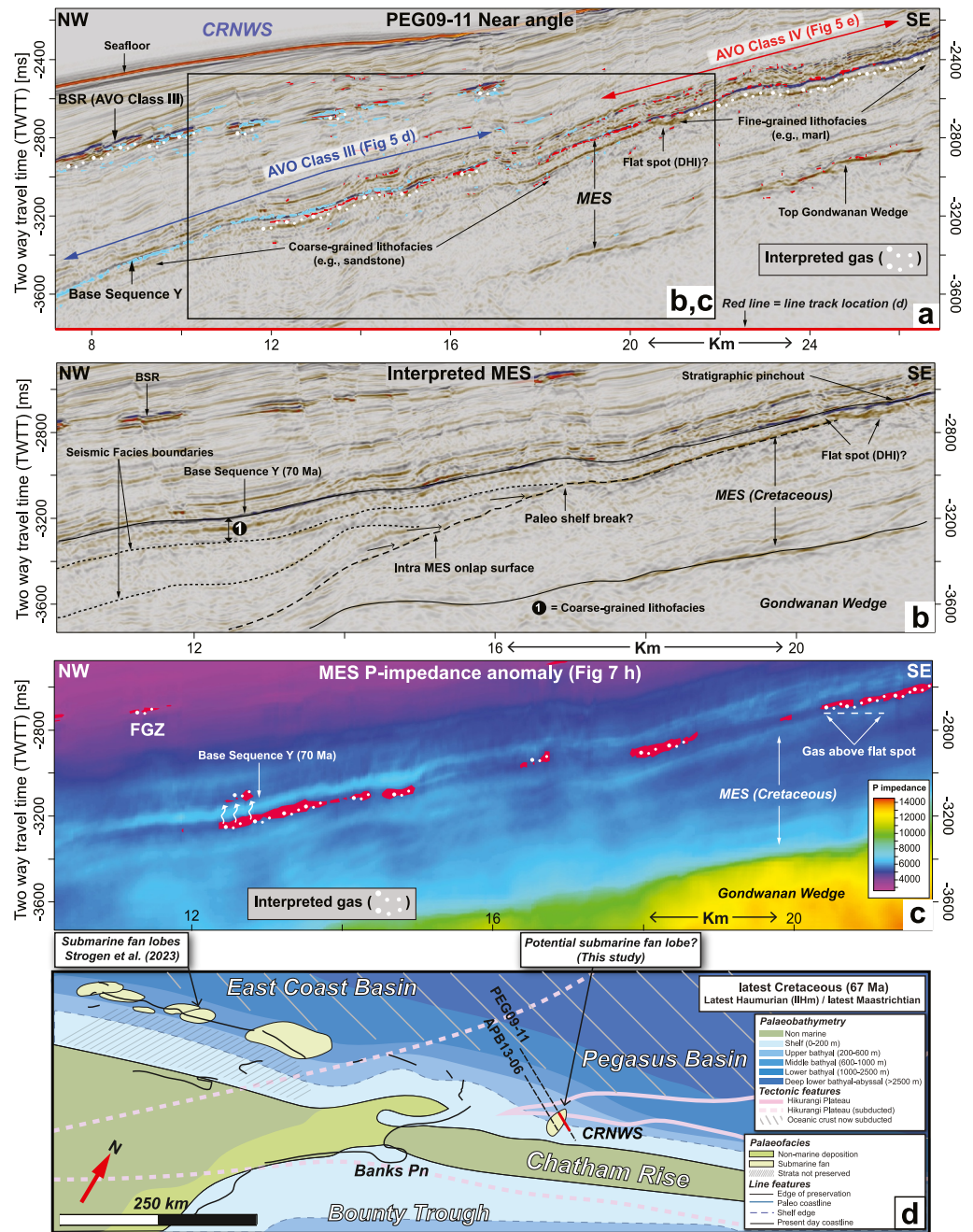
Figure 9. (a) PEG09-11 near-angle with amplitude variation with offset (AVO) classes (cyan points = Class III; red points = Class IV) and free-gas (white dots) interpretations overlain. An approximate lithofacies interpretation is made in the AVO Class IV interval of Mesozoic sedimentary sequence (MES). CRNWS, Chatham Rise northwestern slope; DHI, direct hydrocarbon indicator. Inset window = window (b) and (c) extent. PEG09-11 line location is marked in window (d). (b) Zoomed PEG09-11 near-angle window from window (a) with tentatively interpreted seismic facies boundaries and unconformities marked by black broken lines. Interpretation of coarse-grained lithofacies is shown. (c) PEG09-11 P-impedance section with inversion anomalies (free gas distribution) highlighted in red. Location shown in (a) and Figure 7h. FGZ, Free gas zone. (d) Reconstruction of a Latest Cretaceous paleogeographic map by Strogen et al. (2023) (to approximate scale). We superimpose the approximate locations of APB13-06 and PEG09-11. Red line = extent of window (a). Banks Pn, Banks Peninsula.

with maintained S-impedance, are highlighted in red (Figure 7g). When plotted spatially on the P-impedance section, these red-colored anomalies are localized to the BSR and regions directly under Base Sequence Y (Figure 7h).

3.5. Zoeppritz Modeling

We model co-occurring Class III–IV AVO anomalies observed in PEG09-11 (Figures 5d and 5e). Zoeppritz modeling of a Class III anomaly will sufficiently explain observations made in both PEG09-11 and APB13-06. Figures 8a–8c show three Zoeppritz models used to test the robustness of the method. First, we model an accurate depiction of the seafloor reflection using reasonable parameters for seafloor sediments. A stable P-wave to P-wave (PP) RC until ∼35° AOI is modeled (Figure 8a).

3.5.1. U1520C

IODP U1520C encountered Sequence Y overlying volcaniclastic HKB in the central Hikurangi Trough. We used U1520C-based Vp/Vs ratios, porosity and density values when modeling the Sequence Y chalk layer. We model the direct Base Sequence Y to HKB reflection boundary, otherwise known as the Unit IV to Unit V lithoboundary, occurring at ∼848 mbsf in U1520C (Wallace et al., 2019; Figure 8c). Sequence Y includes a ∼50 m-thick homogeneous interval of nannofossil chalk with ∼45% porosity. Mineralogically, the chalk consists of 95 wt% calcite and ∼5 wt% clay, providing an excellent upper layer analog in our two-layer modeling approach.

HKB directly underlying Sequence Y is volcaniclastic with poor carbonate cementation, resulting in high porosities (∼50%), low Vp (∼1,800 m/s, Vp/Vs = 3.5) and ρ_b (∼1,800 kg/m^3). Modeling this layer boundary resulted in a strong negative normal incidence (NI) RC (−0.245) equal in absolute magnitude to the seafloor and decreasing in absolute RC with AOI (Figure 8c). In this model, the RC reduces by ∼28% from near- to mid-angles (RC 0° = −0.245; RC 32° = −0.18).

As shown in Figure 9b, representative (mean) volcaniclastic HKB Vp (Vp2), Vs (Vs2), and ρ_b (rho2) values were sampled across the upper ∼50 m of U1520C Unit V (IODP, 2018), and were modeled to investigate the impact of porosity and cementation on RCs with AOI. The well-cemented (lower Vp, Vp/Vs = 2.38) U1520C HKB shows a lower NI RC value and a lower (positive) gradient value (Figure 8b).

While CRNWS Base Sequence Y can show localized absolute reflection amplitude parity with the seafloor (e.g., Figure 5j), observed Class IV anomalies in this study do not decrease in absolute amplitude to the same degree (e.g., Figures 3a and 3b). Thus, despite Class IV anomaly modeling in U1520C with poorly cemented volcaniclastic HKB, we do not model a Class III anomaly occurring in U1520C. Our modeling of U1520C generally does not represent what is observed on the CRNWS.

3.5.2. CRNWS MES

Based on previous CRNWS lithologic interpretations (e.g., Bland et al., 2015; Kroeger et al., 2015), we do not expect HKB volcaniclastic deposits in the CRNWS upper MES. As such, we modeled two hypothetical siliciclastic lithologies, which were potentially deposited during the CRNWS's Latest Cretaceous (Bland et al., 2015; Kroeger et al., 2015). We model a marl- and sandstone-based MES.

Low porosity (33%–35%) marls sampled from U1520C, and an approximation of a sandstone-based MES were modeled. With or without the presence of gas, the lower porosity underlying unit (MES analog) was not modeled to replicate AVO observations in the CRNWS (Figure S17 in Supporting Information S1). A high porosity (43%) marl MES (sampled from ∼720 mbsf in U1520C [Unit IV]) produces a clear AVO Class IV anomaly (Figure 8d).

As shown by Castagna et al. (1985) and Ødegaard and Avseth (2003), Vp/Vs is distinctly related to lithology and porosity in brine-bearing rocks. We rely on these Vp/Vs trends, which are partially controlled by the elastic moduli of lithology-specific dominant minerals, to deduce the approximate Vp/Vs of a quartz-dominated sandstone. Typically, an increase in clay content correlates with increased Vp/Vs compared with quartz-dominated sands (Castagna et al., 1985).

As higher Vp/Vs ratios are also tied to strong AVO gradients (Castagna & Swan, 1997), we aim to model the impact of a lower Vp/Vs brine-bearing lithology. One physical basis for asserting a quartz-dominated sand as "low Vp/Vs" is rooted in quartz' shear (μ) and bulk (K) modulus being of near equal value (K = 37 GPa;

$\mu = 44$ GPa). In contrast, clay minerals and calcite exhibit significant disparity between the values of these elastic moduli (Z. Wang, 2001). To model a hypothetical quartz-dominated CRNWS sandstone in the shallowest MES, we model Vp in the range of MES interval velocity (2,300–2,600 m/s) from Davy et al. (2008). We experimented with a range of Vp/Vs ratios from 2.3 to 2.

We find a positive gradient occurs in all brine-saturated modeled MES lithologies, resulting in AVO Class IV anomalies (Figure 9). From Figure 9d, some observations in PEG09-11 could be interpreted as due to a brine-saturated MES underlying Sequence Y. We note that Base Sequence Y in PEG09-11 displayed a Class IV anomaly with NI RCs locally exceeding the strength of the seafloor (e.g., Figures 4a and 5f).

Through Gassmann fluid substitution, we observed the effect of 2%–10% free-gas (methane, 25°C and 10 MPa) substitution within these high-porosity MES models (Figures 8e, 8f, 8h, and 8i). When the brine-saturated marl is fluid substituted with any fraction of gas, we observe NI RCs with absolute values greater than the seafloor RC. We note the persistence of a positive gradient (dimming with angle) in marls, irrespective of the presence of gas at any saturation. Despite the Vp uncertainty of a CRNWS marl and U1520C variability, models suggest that the PEG09-11 Class IV anomaly could result from a brine-bearing marl-based MES underlying Sequence Y.

We model MES as coarse grained, high porosity sandstone (70% quartz, 30% clay) (Figures 8g–8i). The brine-saturated sandstone MES produces a weak negative NI RC with a weakly positive gradient (Figure 8g). Through fluid substitution of 2% free-gas, we calculate a reduction in Vp/Vs from 2.1 to 1.8, which results in a gradient inversion and stronger negative NI RC (Class III anomaly). The weakly negative gradient resulting from gas accurately models observations of absolute amplitude changes with angle in both PEG09-11 and APB13-06 (Figure 3). By modeling several lower Vp/Vs ratios (2.0–2.3), we found that modeling of the negative gradient sign along Base Sequence Y is contingent on the underlying brine-saturated MES having an approximate Vp/Vs ratio of ∼2.1, prior to the substituted inclusion of free-gas. Fundamentally, the presence of 2% free-gas reduces Vp/Vs ratios to ∼1.8, thus producing the observed AVO Class III anomaly.

We model the Class III anomaly as a unique product of gas-related Vp/Vs reduction in a potentially quartz-based lithology, unlike modeled observations made in clay-dominated (higher Vp/Vs) MES. We show how AVO Class III-IV anomalies may concurrently occur at the Base of Sequence Y and both indicate the presence of free gas.

A fundamental limitation of this study is the lack of real MES physical properties. As values are hypothetical and only guided by U1520C and interval velocity information (Davy et al., 2008), we note that the physical properties of the rock frame independent of pore fluid composition could vary strongly from our model inputs. Through modeling, we observed that the Vp/Vs ratios of MES possess a strong control on the RC with AOI, while Vp strongly dictates NI RC (e.g., Castagna & Swan, 1997).

Our models suggest that a brine-bearing lithology with Vp/Vs ratios of ∼1.8 and a Vp of <2,000 m/s would similarly replicate Class III anomalies at the Base of Sequence Y. Although it is currently unclear whether this occurs on the CRNWS, well-cemented HKB volcaniclastics within U1520C showed a mean Vp/Vs of ∼2.38 from 848 to ∼900 mbsf based on our calculations (IODP, 2018; Wallace et al., 2019). Additional support for the presence of gas comes from the interpretation of hydrate BSRs indicative of free gas, and possessing similar Class III AVO anomaly behavior (Figures 9a and 9c). Although mapping BSRs is out of the scope of this study, preliminary observations suggest the presence of deep (>1 km depth) faults spanning the BSR to the intra-MES unit (e.g., Figure S20 in Supporting Information S1; Figure 9a [line km ∼11]).

3.6. Spatially Variable Mesozoic Sedimentary Sequence Lithostratigraphy

Correlating with our along-line variable AVO anomalies, we observed along-line seismic facies changes and a truncating onlap surface within PEG09-11 (Figure 9b). We observe two MES sub-units delineated by an intra-MES unconformity, which appears to truncate or "pinch-out" against Base Sequence Y (Figure 9b). We tentatively interpret the MES sub-unit pinch-out to reflect a change in lithofacies from coarse-grained material in the NW to finer-grained MES in the SE (Figure 9b). A coarsening of lithofacies northwestward, spatially correlating with a stratigraphic pinch-out, provides an explanation for a coincident change from Class IV to III AVO anomaly (Figures 9a and 9b). The northwestwardly thickening upper MES sub-unit may represent a localized lobe of a homogeneous coarse-grained slope fan (e.g., Vail, 1987). To the NW of the study area, the upper MES sub-unit is observed downlapping onto underlying reflections, supporting a localized slope fan interpretation.

At the stratigraphic pinch-out, we observe a horizontal positive polarity reflection, appearing anomalous with respect to the orientation of the apparent stratal dip (Figures 9a and 9b). We interpret this ∼800 m wide horizontal reflection as a potential flat spot/fluid contact between free-gas and water (also known as a direct hydrocarbon indicator).

P- versus S-impedance anomaly data from Figure 7h provide insight into the distribution of free gas within MES (Figure 9c). To the SE, we interpret free-gas occurring above the flat spot (Figure 9c), while down-dip, we interpret a punctuated accumulation of MES-bound free gas. We interpret a small accumulation of free gas above Sequence Y at line km 12. From the almost directly overlying (∼400 ms TWTT) free gas zone P-impedance anomaly, we speculate that vertical fluid connectivity may occur between MES and the gas hydrate stability zone (Figures 9a–9c).

4. Discussion

In the presence of atypical MES lithologies (e.g., poorly cemented volcaniclastics), lithological impedance contrasts alone could result in distinct Class IV AVO anomalies, which partially explain our seismic-AVO observations (e.g., Figure 8c). Similarly, a low Vp/Vs MES at ∼1,100 mbsf (Vp/Vs ∼1.8) with Vp < 2,000 m/s could result in AVO Class III anomalies at the Base of Sequence Y. Under the assumption that a brine-bearing MES is siliciclastic-dominated with a Vp/Vs of 2.1 or higher, we suggest that our seismic-AVO observations do not result from brine-bearing lithological impedance contrasts alone. Thus, we provide two new interpretations of the CRNWS.

4.1. Evidence for Free-Gas Beneath Sequence Y

From AVO modeling, we have observed how free gas effects in siliciclastic MES are primarily expressed by reductions in NI P-wave response (e.g., Foster et al., 2010; Hendrickson, 2001). Due to the "gas effect" on Vp, free-gas saturation in MES can be as low as 2% to produce these profound amplitude-related effects (Domenico, 1977).

Large negative intercept values with a negative gradient (Class III AVO anomaly) observed at the Base of Sequence Y are interpreted as due to the presence of free-gas in a coarse-grained (e.g., sandstone), siliciclastic upper MES. Large negative intercept values with a weakly positive gradient (Class IV AVO anomaly. E.g., Figure 8e) observed at Base Sequence Y are interpreted as due to the presence of free-gas in a fine-grained, siliciclastic upper MES (Castagna et al., 1998). We rule out a volcaniclastic-based MES, which are modeled as Class IV anomalies with strong positive gradient values (e.g., Figure 8c).

Highlighted anomalies in P- and S-impedance sections indicate a reduction in compressional modulus with unchanged shear rigidity (Figure 7h; e.g., Avseth et al., 2016). Impedance anomalies coincide with Class III-IV AVO anomalies and are often explained by considering the discriminate impacts of highly compressible pore fluids such as free-gas on bulk modulus and subsequently P-wave velocity (Goodway et al., 1997; Figures 9a and 9c). We interpret these anomalies as indicative of compartmentalized accumulations of free-gas in the upper MES. To explain along-line variability in AVO anomalies, we consider lithostratigraphic variability within the CRNWS.

Across the study area and to the NW, the sub-Sequence Y MES unit has been previously proposed as gas-bearing near the HSM frontal anticline, and toward the Hikurangi Channel (Crutchley et al., 2020; Hillman et al., 2020; Plaza-Faverola et al., 2012). Although currently undetermined, LVZs thought to mark Pegasus Basin MES free gas (e.g., Crutchley et al., 2020; Plaza-Faverola et al., 2012) may be continuous onto the CRNWS in APB13-06 and PEG09-11, inferring lateral connectivity of Pegasus Basin free gas with the CRNWS.

4.2. Chatham Rise Northwestern Slope Paleogeography

We consider the upper MES' paleo-depositional environment when placing our new lithologic interpretations in the context of the CRNWS. We reconstruct the 2D Latest Cretaceous (67 Ma) paleogeography map originally published by Strogen et al. (2023) (Figure 9d). Lithologically, the MES is thought to fine upward toward the end Cretaceous, controlled by the gradual thermal subsidence and progressive submersion of the CRNWS from the Late Cretaceous (Bland et al., 2015).

Sequence Y's widely published age of 70–32 Ma (Barnes et al., 2010; Davy et al., 2008; Plaza-Faverola et al., 2012) suggests that upper MES deposition occurred at a period when a significant subaerial landmass was situated potentially less than ∼50 km to the south of our study area (Figure 9c). We approximately located PEG09-11 and APB13-06 onto the Latest Cretaceous CRNWS, which demonstrates that our study area was likely within a region that may have been subject to coarse-grained sand deposition (Figure 9d).

Strogen et al. (2023) suggest widespread submarine fan deposition in the Latest Cretaceous East Coast Basin (Figure 9c). Our new lithofacies interpretation of a locally occurring quartz-based MES could provide evidence for the lateral continuity of submarine fan deposition, at least ∼500 km westward into the Latest Cretaceous Pegasus Basin (Figure 9d). We interpolate a tentative interpretation of a sloped submarine fan on the Latest Cretaceous CRNWS for reference (Figure 9d). A southwardly occurring landmass near the CRNWS is mapped until the Late Paleocene (57 Ma). As such, age flexibility in the dating of upper MES and Sequence Y is possible while not invalidating this interpretation.

4.3. Gas Source

Here, we speculate on the varying potential sources of accumulated MES free-gas in the order of most to least likely. Mesophiles, the most productive microbial methanogens, peak in activity within the 35–45°C thermal window of approximately 1,600 mbsf in the Pegasus Basin (B. J. Katz, 2011; Kroeger et al., 2015). However, thermal modeling shows a ∼500 m abiogenic depth window between the base of microbially methanogenic CRNWS strata and the Base of Sequence Y (Kroeger et al., 2015).

Several factors control primary microbial gas generation, which occurs soon after sediment deposition at rates locally dependent on available in situ TOC (Rice, 1993; Waseda, 1998). Favorable methanogenic depositional rates range from 200 to 1,000 m/m.y (Clayton, 1992). At depths >500 m, long-term methanogen activity is thought to range from ∼4.3 to ∼20 Myr at most (Cragg et al., 1992; Fishman et al., 2001; Lillis, 2007). Noble and Henk (1998) suggest that methanogen activity can continue for 5–6 Myr after emplacement and recharge structurally compromised reservoirs with a substantial volume of biogenic methane long after initial burial. When factoring the age variability of upper MES (∼70 to ∼58 Ma), primary biogenic methanogenesis could have continued conservatively into the Early Eocene (∼54 Ma) or at most into the Late Eocene (∼38 Ma).

The effective sealing of MES-derived biogenic methane is contingent on the presence of stratigraphically continuous, fine-grained sediments (Downey, 1987; Rice, 1993). As the broader lithologic character of MES is poorly understood, we cannot confidently assume the presence of tight intra-MES sealing intervals. The presence of overlying Sequence Y chalks and calcareous mudstones suggests that the MES is likely stratigraphically sealed today (Davy et al., 2008; Dutilleul et al., 2020); however, the degree to which Sequence Y acts as a seal is yet unknown across the HSM (Crutchley et al., 2020).

Rice and Claypool (1981) note the necessity of an effective seal and trap existing prior to the release of gas from solution, which does not typically occur until sediments have been buried to depths greater than 500 m. Thus, it is possible that older methanogenic MES material, which directly overlies the Gondwanan wedge, did not have an effective overlying stratigraphic seal during burial. The lack of intra-MES AVO anomalies suggests that no obvious deeper trapping of free-gas occurs. Thus, while long-term "trapping" of ancient biogenic free-gas may be likely on the CRNWS, gases are probably sourced from the upper ∼500 m of MES.

Although primary microbial activity within MES is unlikely today, secondary microbial methanogenesis may be possible, dependent on the occurrence of organic-rich shales or migrated oil accumulations, which sustain long-term microbial metabolic activity (e.g., Arndt et al., 2006; Krumholz et al., 1997; Milkov, 2011). In a marine context, secondary microbial methanogenesis would be contingent on the biodegradation of a deeply sourced high TOC (∼85%) food source (e.g., oil). The speculation of localized biodegradation of black shales (e.g., Arndt et al., 2006) or secondary microbial methanogenesis (e.g., Milkov, 2011) implies the potential of thermogenic methane as being the primary type of accumulating gas.

4.3.1. Thermogenic Free-Gas

At a depth of ∼12–13 km within the southern HSM's subduction window, Kroeger et al. (2015) model a thermogenic methane window. The subducting MES is posited to host "shaley" (∼0.5%–5% TOC) source-rock intervals (e.g., Waipawa Formation or the Te Uri Member), which may have expelled a significant volume of gas

during burial. Up to 800–1,100 megatons are predicted to have been generated across a 100 km^2 area since the Miocene to the Recent (Kroeger et al., 2015). Plaza-Faverola et al. (2012) speculated on the contribution of thermogenic free gas toward the enrichment of gas hydrate deposits at the deformation front and adjacent to the Hikurangi Channel. Kroeger et al. (2015, 2019) support these speculations, with the resulting hydrate-accumulation models being potentially indicative of long-distance migration of thermogenic free-gas.

As Kroeger et al. (2019) highlight the preferential migration of thermogenic gases into the mantling trench strata, CRNWS accumulation of thermogenic free-gas would imply a longer-distance migration of gases than was previously expected (∼50 km further oceanward of the deformation front). Although the potential of thermogenic MES gas migration is unclear, preliminary deeper angle-stack observations of Base Sequence Y show anomalous far-angle "brightening," worthy of more detailed investigation (e.g., Figure 2c). At present, we speculate that thermogenic gases are likely to accumulate on the CRNWS under Sequence Y.

4.3.2. Sub Gondwanan Wedge

As the gas-bearing MES directly mantles a >6 km-thick accretionary wedge (Figures 1b and 9b), a previously unexplored source of free-gas may stem from any unmetamorphosed deep (up to ∼10 km) strata within the fossil subduction complex (Figure 1b). Eastward along the Chatham Rise, the former East Gondwanan subduction margin is not currently thought to feature an underthrusted sedimentary sequence (e.g., Davy et al., 2008). Despite this, the accretionary wedge is posited to overlie an underplated Cretaceous-aged sedimentary sequence in PEG09-19 (Bland et al., 2015), which is stratigraphically contiguous with MES NW of the wedge (oceanward of the Gondwanan deformation front). We speculate that thermogenic gas generation at the base of the Gondwanan wedge may have occurred as early as the Mesozoic, which implies a long-standing thermogenic system.

Our study has predicted the occurrence of free gas within the MES unit, deep (>1 km) beneath the CRNWS, and highlighted previously unknown lithological variability within the unit. Further research is required to determine the origin of the gas, its emplacement into the MES unit, and the nature of trapping. These considerations are important for understanding the hydrological properties of the MES unit and the overlying Sequence Y, which have implications for the development of the active Hikurangi subduction interface further landward.

5. Conclusions

We have used two long-offset seismic reflection surveys to conduct a Shuey (1985) 2-term AVO analysis and simultaneous AVO inversion (Ma, 2002) on the Chatham Rise northwestern slope located at the southern end of the Hikurangi subduction margin (HSM). The Base of the Sequence Y chalk interval and nearby hydrate-BSR were characterized as Class III-IV AVO anomalies, unified through their strong negative intercept amplitudes.

AVO-Zoeppritz modeling with inverted P- and S-impedance models supports the interpretation of accumulated free gas present in both coarse- and fine-grained upper MES strata. Strong negative intercept amplitudes are likely indicative of trapped free-gas, with the AVO anomaly's gradient sign being indicative of MES lithology. Class III anomalies (negative gradient sign) are uniquely modeled to represent coarse-grained, free-gas-bearing MES. We interpret Class III anomalies to mark the presence of a previously undefined coarse-grained/sandy lithofacies deposited within large slope submarine fans on the Latest Cretaceous to Early Paleocene CRNWS.

The source of gas is presently unclear; however, upper MES gas is potentially derived from ancient methanogens or supplied from beneath the NW-neighboring Hikurangi Trough. As free gas accumulations directly overlie a thick (>6 km) ancient East Gondwanan subduction complex, our interpretations may be indicative of a new thermogenic gas system related to the >100 Ma subduction of carbon-rich MES source rocks, which today expels gas beneath the southern HSM. The presence of gas related to sub-Gondwanan wedge methanogenesis would highlight the northwestern Chatham Rise as an ancient Gondwanan thermogenic system. Further basin modeling should be done to constrain the potential volume of free gas, and deep stratigraphic interpretation focused on deep Gondwanan wedge itself.

Data Availability Statement

Seismic data used in this study are publicly accessible through https://geodata.nzpam.govt.nz/. IODP U1520C borehole data can be accessed through https://brg.ldeo.columbia.edu/data/iodp-usio/exp375/U1520C/.

References

Al-Khateb, N. (2018). Gassmann's fluid substitution (v1.3) [Windows application]. Retrieved from https://gassmanns-fluid-substitution.en.softonic.com/

Andreassen, K., Hart, P. E., & MacKay, M. (1997). Amplitude versus offset modeling of the bottom simulating reflection associated with submarine gas hydrates. *Marine Geology*, *137*(1–2), 25–40. https://doi.org/10.1016/s0025-3227(96)00076-x

Arndt, S., Brumsack, H. J., & Wirtz, K. W. (2006). Cretaceous black shales as active bioreactors: A biogeochemical model for the deep biosphere encountered during ODP Leg 207 (Demerara Rise). *Geochimica et Cosmochimica Acta*, *70*(2), 408–425. https://doi.org/10.1016/j.gca.2005.09.010

Avseth, P., Janke, A., & Horn, F. (2016). AVO inversion in exploration—Key learnings from a Norwegian Sea prospect. *The Leading Edge*, *35*(5), 405–414. https://doi.org/10.1190/tle35050405.1

Barnes, P. M. (1994a). Continental extension of the Pacific Plate at the southern termination of the Hikurangi subduction zone: The North Mernoo Fault Zone, offshore New Zealand. *Tectonics*, *13*(4), 735–754. https://doi.org/10.1029/94tc00798

Barnes, P. M. (1994b). Pliocene-Pleistocene depositional units on the continental slope off central New Zealand: Control by slope currents and global climate cycles. *Marine Geology*, *117*(1–4), 155–175. https://doi.org/10.1016/0025-3227(94)90012-4

Barnes, P. M., Lamarche, G., Bialas, J., Henrys, S., Pecher, I., Netzeband, G. L., et al. (2010). Tectonic and geological framework for gas hydrates and cold seeps on the Hikurangi subduction margin, New Zealand. *Marine Geology*, *272*(1–4), 26–48. https://doi.org/10.1016/j.margeo.2009.03.012

Beavan, J., & Haines, J. (2001). Contemporary horizontal velocity and strain rate fields of the Pacific-Australian plate boundary zone through New Zealand. *Journal of Geophysical Research*, *106*(B1), 741–770. https://doi.org/10.1029/2000jb900302

Bland, K. J., Uruski, C. I., & Isaac, M. J. (2015). Pegasus Basin, eastern New Zealand: A stratigraphic record of subsidence and subduction, ancient and modern. *New Zealand Journal of Geology and Geophysics*, *58*(4), 319–343. https://doi.org/10.1080/00288306.2015.1076862

Cambois, G. (1998). AVO attributes and noise: Pitfalls of crossplotting. In *SEG technical program expanded abstracts 1998* (pp. 244–247). Society of Exploration Geophysicists.

Cambois, G. (2000). Can P-wave AVO be quantitative? *The Leading Edge*, *19*(11), 1246–1251. https://doi.org/10.1190/1.1438516

Campbell, K. A., Francis, D. A., Collins, M., Gregory, M. R., Nelson, C. S., Greinert, J., & Aharon, P. (2008). Hydrocarbon seep-carbonates of a Miocene forearc (East Coast Basin), North Island, New Zealand. *Sedimentary Geology*, *204*(3–4), 83–105. https://doi.org/10.1016/j.sedgeo.2008.01.002

Carter, R. M., McCave, I. N., Richter, C., Carter, C., et al. (1999). Site 1124; Rekohu Drift; from the K/T boundary to the Deep Western Boundary Current. Initial reports; Southwest Pacific gateways; covering Leg 181 of the cruises of the drilling vessel JOIDES Resolution; Sydney, Australia, to Wellington, New Zealand; sites 1119–1125; 11 August–8 October 1998, Proceedings of the Ocean Drilling Program Initial Reports 181. In *Proceedings of the Ocean Drilling Program* (p. 137).

Castagna, J. P., Batzle, M. L., & Eastwood, R. L. (1985). Relationships between compressional-wave and shear-wave velocities in clastic silicate rocks. *Geophysics*, *50*(4), 571–581. https://doi.org/10.1190/1.1441933

Castagna, J. P., & Smith, S. W. (1994). Comparison of AVO indicators: A modeling study. *Geophysics*, *59*(12), 1849–1855. https://doi.org/10.1190/1.1443572

Castagna, J. P., & Swan, H. W. (1997). Principles of AVO crossplotting. *The Leading Edge*, *16*(4), 337–344. https://doi.org/10.1190/1.1437626

Castagna, J. P., Swan, H. W., & Foster, D. J. (1998). Framework for AVO gradient and intercept interpretation. *Geophysics*, *63*(3), 948–956. https://doi.org/10.1190/1.1444406

CGG Services (Singapore) Pte. Ltd/Anadarko New Zealand Company. (2014a). *PEP54858 and PEP 54861 PEG09 PSTM reprocessing report 2014*. New Zealand Unpublished Petroleum Report PR4959. NZP&M, Ministry of Business, Innovation & Employment (MBIE).

CGG Services (Singapore) Pte. Ltd/Anadarko New Zealand Company. (2014b). *Seismic data processing report—APB-13-2D Pegasus Basin 2D PEP54861*. New Zealand Unpublished Petroleum Report PR5170. NZP&M, Ministry of Business Innovation & Employment (MBIE).

Chopra, S., & Castagna, J. P. (2014). *Avo*. Society of Exploration Geophysicists.

Clairmont, R., Bedle, H., Marfurt, K., & Wang, Y. (2021). Seismic attribute analyses and attenuation applications for detecting gas hydrate presence. *Geosciences*, *11*(11), 450. https://doi.org/10.3390/geosciences11110450

Clayton, C. (1992). Source volumetrics of biogenic gas generation. In *Bacterial gas: Proceedings of the conference held in Milan, September 25–26, 1989* (p. 191). Editions Technip. Retrieved from https://books.google.co.nz/books?hl=en&lr=&id=KlgXcF1NtFoC&oi=fnd&pg=PA191&dq=Clayton+1992+deposition+rates+methanogenesis&ots=yyZk0hvQeh&sig=qEJ5r4C6W7a1ms6f2mDo_nPRg50&redir_esc=y#v=onepage&q=Clayton%201992%20deposition%20rates%20methanogenesis&f=false

Cragg, B. A., Harvey, S. M., Fry, J. C., Herbert, R. A., & Parkes, R. J. (1992). 46. Bacterial biomass and activity in the deep sediment layers of the Japan Sea, Hole 798B. *Proceedings of the Ocean Drilling Program, Scientific Results*, *127*(128), 761–776.

Crutchley, G. J., Klaeschen, D., Henrys, S. A., Pecher, I. A., Mountjoy, J. J., & Woelz, S. (2020). Subducted sediments, upper-plate deformation and dewatering at New Zealand's southern Hikurangi subduction margin. *Earth and Planetary Science Letters*, *530*, 115945. https://doi.org/10.1016/j.epsl.2019.115945

Crutchley, G. J., Kroeger, K. F., Pecher, I. A., & Gorman, A. R. (2019). How tectonic folding influences gas hydrate formation: New Zealand's Hikurangi subduction margin. *Geology*, *47*(1), 39–42. https://doi.org/10.1130/g45151.1

Davy, B. (2014). Rotation and offset of the Gondwana convergent margin in the New Zealand region following Cretaceous jamming of Hikurangi Plateau large igneous province subduction. *Tectonics*, *33*(8), 1577–1595. https://doi.org/10.1002/2014tc003629

Davy, B., Hoernle, K., & Werner, R. (2008). Hikurangi Plateau: Crustal structure, rifted formation, and Gondwana subduction history. *Geochemistry, Geophysics, Geosystems*, *9*(7), Q07004. https://doi.org/10.1029/2007gc001855

de Macedo, I. A. S., da Silva, C. B., & de Figueiredo, J. J. S. (2016). Comparison of deterministic wavelet estimation and statistic wavelet estimation through predictive deconvolution on the quality of well tie: Application on synthetic and real data.

DeMets, C., Gordon, R. G., & Argus, D. F. (2010). Geologically current plate motions. *Geophysical Journal International*, *181*(1), 1–80. https://doi.org/10.1111/j.1365-246x.2009.04491.x

Domenico, S. N. (1977). Elastic properties of unconsolidated porous sand reservoirs. *Geophysics*, *42*(7), 1339–1368. https://doi.org/10.1190/1.1440797

Downey, M. W. (1987). Evaluating seals for hydrocarbon accumulations. *AAPG Bulletin*, *71*(11), 1439–1440.

Dutilleul, J., Bourlange, S., Géraud, Y., & Stemmelen, D. (2020). Porosity, pore structure, and fluid distribution in the sediments entering the northern Hikurangi margin, New Zealand. *Journal of Geophysical Research: Solid Earth*, *125*(11), e2020JB020330. https://doi.org/10.1029/2020jb020330

Fatti, J. L., Smith, G. C., Vail, P. J., Strauss, P. J., & Levitt, P. R. (1994). Detection of gas in sandstone reservoirs using AVO analysis: A 3-D seismic case history using the Geostack technique. *Geophysics*, *59*(9), 1362–1376. https://doi.org/10.1190/1.1443695

Fishman, N. S., Ridgley, J. L., & Hall, D. L. (2001). Timing of gas generation in the cretaceous milk river formation, Southeastern Alberta and Southwestern Saskatchewan–evidence from authigenic carbonates. *Summary of Investigations*, *1*, 125–136.

Fohrmann, M., & Pecher, I. A. (2012). Analysing sand-dominated channel systems for potential gas-hydrate-reservoirs using an AVO seismic inversion technique on the Southern Hikurangi Margin, New Zealand. *Marine and Petroleum Geology*, *38*(1), 19–34. https://doi.org/10.1016/j.marpetgeo.2012.08.001

Foster, D. J., Keys, R. G., & Lane, F. D. (2010). Interpretation of AVO anomalies. *Geophysics*, *75*(5), 75A3–75A13. https://doi.org/10.1190/1.3467825

Galvez, M. E., & Pubellier, M. (2019). How do subduction zones regulate the carbon cycle? In B. N. Orcutt, I. Daniel, & R. Dasgupta (Eds.), *Deep carbon: Past to present* (pp. 276–312). Cambridge University Press.

Gardner, G. H. F., Gardner, L. W., & Gregory, A. (1974). Formation velocity and density—The diagnostic basics for stratigraphic traps. *Geophysics*, *39*(6), 770–780. https://doi.org/10.1190/1.1440465

Gassmann, F. (1951). Elastic waves through a packing of spheres. *Geophysics*, *16*(4), 673–685. https://doi.org/10.1190/1.1437718

Goodway, B., Chen, T., & Downton, J. (1997). Improved AVO fluid detection and lithology discrimination using Lamé petrophysical parameters; "λρ", "μρ", & "λ/μ fluid stack", from P and S inversions. In *SEG technical program expanded abstracts 1997* (pp. 183–186). Society of Exploration Geophysicists.

Hendrickson, J. S. (2001). Stacked. *Geophysical Prospecting*, *47*(5), 663–706. https://doi.org/10.1046/j.1365-2478.1999.00150.x

Hessler, A. M., & Sharman, G. R. (2018). Subduction zones and their hydrocarbon systems. *Geosphere*, *14*(5), 2044–2067. https://doi.org/10.1130/ges01656.1

Hillman, J. I., Crutchley, G. J., & Kroeger, K. F. (2020). Investigating the role of faults in fluid migration and gas hydrate formation along the southern Hikurangi Margin, New Zealand. *Marine Geophysical Researches*, *41*(1), 8. https://doi.org/10.1007/s11001-020-09400-2

IODP. (2018). Dipole sonic imager – Main pass. (Published data). Standard Data file index IODP Expedition 375 – Hole U1520C. Retrieved from https://brg.ldeo.columbia.edu/data/iodpusio/exp375/U1520C/standard/index_standard.html

Katz, B. J. (2011). Microbial processes and natural gas accumulations. *The Open Geology Journal*, *5*(1), 75–83. https://doi.org/10.2174/1874262901105010075

Katz, H. R. (1981). Probable gas hydrate in continental slope east of the North Island, New Zealand. *Journal of Petroleum Geology*, *3*(3), 315–324. https://doi.org/10.1111/j.1747-5457.1981.tb00933.x

Kroeger, K. F., Crutchley, G. J., Hillman, J. I., Turco, F., & Barnes, P. M. (2022). Gas hydrate formation beneath thrust ridges: A test of concepts using 3D modelling at the southern Hikurangi Margin, New Zealand. *Marine and Petroleum Geology*, *135*, 105394. https://doi.org/10.1016/j.marpetgeo.2021.105394

Kroeger, K. F., Crutchley, G. J., Kellett, R., & Barnes, P. M. (2019). A 3-D model of gas generation, migration, and gas hydrate formation at a Young Convergent Margin (Hikurangi Margin, New Zealand). *Geochemistry, Geophysics, Geosystems*, *20*(11), 5126–5147. https://doi.org/10.1029/2019gc008275

Kroeger, K. F., di Primio, R., & Horsfield, B. (2011). Atmospheric methane from organic carbon mobilization in sedimentary basins—The sleeping giant? *Earth-Science Reviews*, *107*(3–4), 423–442. https://doi.org/10.1016/j.earscirev.2011.04.006

Kroeger, K. F., Plaza-Faverola, A., Barnes, P. M., & Pecher, I. A. (2015). Thermal evolution of the New Zealand Hikurangi subduction margin: Impact on natural gas generation and methane hydrate formation–A model study. *Marine and Petroleum Geology*, *63*, 97–114. https://doi.org/10.1016/j.marpetgeo.2015.01.020

Krumholz, L. R., McKinley, J. P., Ulrich, G. A., & Suflita, J. M. (1997). Confined subsurface microbial communities in Cretaceous rock. *Nature*, *386*(6620), 64–66. https://doi.org/10.1038/386064a0

Lewis, K. B., Collot, J. Y., & Lallem, S. E. (1998). The dammed Hikurangi Trough: A channel-fed trench blocked by subducting seamounts and their wake avalanches (New Zealand–France GeodyNZ Project). *Basin Research*, *10*(4), 441–468. https://doi.org/10.1046/j.1365-2117.1998.00080.x

Lillis, P. G. (2007). Upper Cretaceous microbial petroleum systems in north-central Montana. *Mountain Geologist*, *44*(N1), 11–35.

Ma, X. Q. (2002). Simultaneous inversion of prestack seismic data for rock properties using a global simulated annealing. *Geophysics*, *67*(6), 1877–1885. https://doi.org/10.1190/1.1527087

McArthur, A. D., Bailleul, J., Mahieux, G., Claussmann, B., Wunderlich, A., & McCaffrey, W. D. (2021). Deformation–sedimentation feedback and the development of anomalously thick aggradational turbidite lobes: Outcrop and subsurface examples from the Hikurangi Margin, New Zealand. *Journal of Sedimentary Research*, *91*(4), 362–389. https://doi.org/10.2110/jsr.2020.013

Milkov, A. V. (2011). Worldwide distribution and significance of secondary microbial methane formed during petroleum biodegradation in conventional reservoirs. *Organic Geochemistry*, *42*(2), 184–207. https://doi.org/10.1016/j.orggeochem.2010.12.003

Mitchum, R. M., Jr., Vail, P. R., & Thompson, S., III. (1977). Seismic stratigraphy and global changes of sea level: Part 2. The depositional sequence as a basic unit for stratigraphic analysis: Section 2. Application of seismic reflection configuration to stratigraphic interpretation (AAPG Memoir 26). In C. E. Payton (Ed.), *Seismic stratigraphy—Applications to hydrocarbon exploration* (pp. 53–62). American Association of Petroleum Geologists.

Moore, J. C., & Vrolijk, P. (1992). Fluids in accretionary prisms. *Reviews of Geophysics*, *30*(2), 113–135. https://doi.org/10.1029/92rg00201

Mortimer, N., van den Bogaard, P., Hoernle, K., Timm, C., Gans, P. B., Werner, R., & Riefstahl, F. (2019). Late Cretaceous oceanic plate reorganization and the breakup of Zealandia and Gondwana. *Gondwana Research*, *65*, 31–42. https://doi.org/10.1016/j.gr.2018.07.010

Noble, R. A., & Henk, F. H., Jr. (1998). Hydrocarbon charge of a bacterial gas field by prolonged methanogenesis: An example from the East Java Sea, Indonesia. *Organic Geochemistry*, *29*(1–3), 301–314. https://doi.org/10.1016/s0146-6380(98)00064-3

Ødegaard, E. R. I. K., & Avseth, P. (2003). Interpretation of elastic inversion results using rock physics templates. In *65th EAGE conference & exhibition* (p. cp-6). European Association of Geoscientists & Engineers.

ODP Leg 110 Scientific Party. (1987). Expulsion of fluids from depth along a subduction-zone decollement horizon. *Nature*, *326*(6115), 785–788. https://doi.org/10.1038/326785a0

Ostrander, W. J. T. (1984). Plane-wave reflection coefficients for gas sands at nonnormal angles of incidence. *Geophysics*, *49*(10), 1637–1648. https://doi.org/10.1190/1.1441571

Pecher, I. A., Henrys, S. A., Wood, W. T., Kukowski, N., Crutchley, G. J., Fohrmann, M., et al. (2010). Focussed fluid flow on the Hikurangi Margin, New Zealand—Evidence from possible local upwarping of the base of gas hydrate stability. *Marine Geology*, *272*(1–4), 99–113. https://doi.org/10.1016/j.margeo.2009.10.006

Plaza-Faverola, A., Henrys, S., Pecher, I., Wallace, L., & Klaeschen, D. (2016). Splay fault branching from the Hikurangi subduction shear zone: Implications for slow slip and fluid flow. *Geochemistry, Geophysics, Geosystems*, *17*(12), 5009–5023. https://doi.org/10.1002/2016gc006563

Plaza-Faverola, A., Klaeschen, D., Barnes, P., Pecher, I., Henrys, S., & Mountjoy, J. (2012). Evolution of fluid expulsion and concentrated hydrate zones across the southern Hikurangi subduction margin, New Zealand: An analysis from depth migrated seismic data. *Geochemistry, Geophysics, Geosystems*, *13*(8), Q08018. https://doi.org/10.1029/2012gc004228

Poreda, R. J., Jeffrey, A. W. A., Kaplan, I. R., & Craig, H. (1988). Magmatic helium in subduction-zone natural gases. *Chemical Geology*, *71*(1–3), 199–210. https://doi.org/10.1016/0009-2541(88)90115-5

Reflect Geophysical Pte Ltd. (2010). *Marine acquisition report—Ministry of Economic Development, New Zealand Pegasus, SAKHE and Bounty Trough 2D Marine Seismic Surveys*. New Zealand Unpublished Petroleum Report PR4158. NZP&M, Ministry of Business Innovation & Employment (MBIE).

Rice, D. D. (1993). *Biogenic gas: Controls, habitats, and resource potential* (p. 1570). Professional Paper. United States Geological Survey.

Rice, D. D., & Claypool, G. E. (1981). Generation, accumulation, and resource potential of biogenic gas. *AAPG Bulletin*, *65*(1), 5–25. https://doi.org/10.1306/2f919765-16ce-11d7-8645000102c1865d

Ring, U., Mortimer, N., & Deckert, H. (2019). Critical-wedge theory and the Mesozoic accretionary wedge of New Zealand. *Journal of Structural Geology*, *122*, 1–10. https://doi.org/10.1016/j.jsg.2019.02.005

Robertson, A. H., Campbell, H. J., Johnston, M. R., & Palamakumbra, R. (2019). Construction of a Paleozoic–Mesozoic accretionary orogen along the active continental margin of SE Gondwana (South Island, New Zealand): Summary and overview. In A. H. F. Robertson (Ed.), *Paleozoic–Mesozoic Geology of South Island, New Zealand: Subduction-related processes adjacent to SE Gondwana*. https://doi.org/10.1144/M49.8

Rutherford, S. R., & Williams, R. H. (1989). Amplitude-versus-offset variations in gas sands. *Geophysics*, *54*(6), 680–688. https://doi.org/10.1190/1.1442696

Sangree, J. B., & Widmier, J. M. (1977). Seismic stratigraphy and global changes of sea level: Part 9. Seismic interpretation of clastic depositional facies: Section 2. Application of seismic reflection configuration to stratigraphic interpretation (AAPG Memoir 26). In C. E. Payton (Ed.), *Seismic stratigraphy—Applications to hydrocarbon exploration* (pp. 165–184). American Association of Petroleum Geologists.

Scheirer, A. H., Tennyson, M. E., Magoon, L. B., Charpentier, R. R., Cook, T. A., Klett, T. R., et al. (2006). Assessment of undiscovered natural gas resources of the Sacramento Basin province of California, 2006. U.S. Geological Survey National Assessment of Oil and Gas Fact Sheet (p. 2).

Schoell, M. (1988). Multiple origins of methane in the Earth. *Chemical Geology*, *71*(1–3), 1–10. https://doi.org/10.1016/0009-2541(88)90101-5

Shuey, R. T. (1985). A simplification of the Zoeppritz equations. *Geophysics*, *50*(4), 609–614. https://doi.org/10.1190/1.1441936

Simm, R. (2007). Practical Gassmann fluid substitution in sand/shale sequences. *First Break*, *25*(12), 61–68. https://doi.org/10.3997/1365-2397.2007030

Singh, S. C., Minshull, T. A., & Spence, G. D. (1993). Velocity structure of a gas hydrate reflector. *Science*, *260*(5105), 204–207. https://doi.org/10.1126/science.260.5105.204

Smith, G. C., & Gidlow, P. M. (1987). Weighted stacking for rock property estimation and detection of gas. *Geophysical Prospecting*, *35*(9), 993–1014. https://doi.org/10.1111/j.1365-2478.1987.tb00856.x

Stanley, R. G., Pierce, B. S., & Houseknecht, D. W. (2011). U.S. Geological Survey 2011 assessment of undiscovered oil and gas resources of the Cook Inlet Region, south-central Alaska. U.S. Geological Survey Open-File Report, 2011-1237 (p. 37).

Stolper, D. A., Lawson, M., Davis, C. L., Ferreira, A. A., Neto, E. S., Ellis, G. S., et al. (2014). Formation temperatures of thermogenic and biogenic methane. *Science*, *344*(6191), 1500–1503. https://doi.org/10.1126/science.1254509

Strogen, D. P., Seebeck, H., Hines, B. R., Bland, K. J., & Crampton, J. S. (2023). Palaeogeographic evolution of Zealandia: Mid-Cretaceous to present. *New Zealand Journal of Geology and Geophysics*, *66*(3), 528–557. https://doi.org/10.1080/00288306.2022.2115520

Suzuki, N., Koike, K., Kameda, J., & Kimura, G. (2024). Thermogenic methane and hydrogen generation in subducted sediments of the Nankai Trough. *Communications Earth & Environment*, *5*(1), 97. https://doi.org/10.1038/s43247-024-01252-7

Swan, H. W., Castagna, J. P., & Backus, M. M. (1993). Properties of direct AVO hydrocarbon indicators. In *Offset dependent reflectivity–Theory and practice of AVO anomalies*, *Investigations in Geophysics, No. 8* (pp. 78–92).

Turco, F., Crutchley, G. J., Gorman, A. R., Mountjoy, J. J., Hillman, J. I., & Woelz, S. (2020). Seismic velocity and reflectivity analysis of concentrated gas hydrate deposits on the southern Hikurangi Margin (New Zealand). *Marine and Petroleum Geology*, *120*, 104572. https://doi.org/10.1016/j.marpetgeo.2020.104572

Turco, F., Ladroit, Y., Watson, S. J., Seabrook, S., Law, C. S., Crutchley, G. J., et al. (2022). Estimates of methane release from gas seeps at the Southern Hikurangi Margin, New Zealand. *Frontiers in Earth Science*, *10*, 834047. https://doi.org/10.3389/feart.2022.834047

Vail, P. R. (1987). Seismic stratigraphy interpretation using sequence stratigraphy: Part 1: Seismic stratigraphy interpretation procedure.

van de Lagemaat, S. H., Kamp, P. J., Boschman, L. M., & Van Hinsbergen, D. J. (2023). Reconciling the Cretaceous breakup and demise of the Phoenix Plate with East Gondwana orogenesis in New Zealand. *Earth-Science Reviews*, *236*, 104276. https://doi.org/10.1016/j.earscirev.2022.104276

von Huene, R., & Scholl, D. W. (1991). Observations at convergent margins concerning sediment subduction, subduction erosion, and the growth of continental crust. *Reviews of Geophysics*, *29*(3), 279–316. https://doi.org/10.1029/91rg00969

Wallace, L. M., Barnes, P., Beavan, J., Van Dissen, R., Litchfield, N., Mountjoy, J., et al. (2012). The kinematics of a transition from subduction to strike-slip: An example from the central New Zealand plate boundary. *Journal of Geophysical Research*, *117*(B2), B02405. https://doi.org/10.1029/2011jb008640

Wallace, L. M., Beavan, J., McCaffrey, R., & Darby, D. (2004). Subduction zone coupling and tectonic block rotations in the North Island, New Zealand. *Journal of Geophysical Research*, *109*(B12), B12406. https://doi.org/10.1029/2004jb003241

Wallace, L. M., Saffer, D. M., Barnes, P. M., Pecher, I. A., Petronotis, K. E., LeVay, L. J., et al. (2019). Expedition 372B/375 methods. In L. M. Wallace, D. M. Saffer, P. M. Barnes, I. A. Pecher, K. E. Petronotis, L. J. LeVay, & and the Expedition 372/375 Scientists (Eds.), *Hikurangi subduction margin coring, logging, and observatories. Proceedings of the International Ocean Discovery Program, 372B/375*. (International Ocean Discovery Program).

Wallmann, K., Pinero, E., Burwicz, E., Haeckel, M., Hensen, C., Dale, A., & Ruepke, L. (2012). The global inventory of methane hydrate in marine sediments: A theoretical approach. *Energies*, *5*(7), 2449–2498. https://doi.org/10.3390/en5072449

Wang, X., & Pan, D. (2017). Application of AVO attribute inversion technology to gas hydrate identification in the Shenhu Area, South China Sea. *Marine and Petroleum Geology*, *80*, 23–31. https://doi.org/10.1016/j.marpetgeo.2016.11.015

Wang, Z. (2001). Y2K Tutorial: Fundamentals of seismic rock physics. *Geophysics*, *66*(2), 398–412. https://doi.org/10.1190/1.1444931

Warnke, F. (2022a). Convert_seismic_velocities.py. [Python script]. Retrieved from https://gist.github.com/fwrnke/9003923cbb7b3941c2b01c6ecfbd7206

Warnke, F. (2022b). segy-crooked2D-to-pseudo3D. [Python script]. Retrieved from https://github.com/fwrnke/segy-crooked2D-to-pseudo3D

Waseda, A. (1998). Organic carbon content, bacterial methanogenesis, and accumulation processes of gas hydrates in marine sediments. *Geochemical Journal*, *32*(3), 143–157. https://doi.org/10.2343/geochemj.32.143

Watson, S. J., Mountjoy, J. J., Barnes, P. M., Crutchley, G. J., Lamarche, G., Higgs, B., et al. (2020). Focused fluid seepage related to variations in accretionary wedge structure, Hikurangi margin, New Zealand. *Geology*, *48*(1), 56–61. https://doi.org/10.1130/g46666.1

Welte, D. H. (1965). Relation between petroleum and source rock. *AAPG Bulletin*, *49*(12), 2246–2268. https://doi.org/10.1306/a663388c-16c0-11d7-8645000102c1865d

Wood, R., & Davy, B. (1994). The Hikurangi Plateau. *Marine Geology*, *118*(1–2), 153–173. https://doi.org/10.1016/0025-3227(94)90118-x

Young, R. A., & LoPiccolo, R. D. (2003). A comprehensive AVO classification. *The Leading Edge*, *22*(10), 1030–1037. https://doi.org/10.1190/1.1623645

Zoeppritz, K. (1919). Erdbebenwellen VIII B, Uber Reflexion und Durchgang seismischer Wellen durch Unstetigkeisflachen. *Gottinger Nachr*, *1*, 66–84.

References From the Supporting Information

Carter, L., & McCave, I. N. (1994). Development of sediment drifts approaching an active plate margin under the SW Pacific Deep Western Boundary Current. *Paleoceanography*, *9*(6), 1061–1085. https://doi.org/10.1029/94pa01444

Joyce, J. E., Tjalsma, L. R., & Prutzman, J. M. (1990). High-resolution planktic stable isotope record and spectral analysis for the last 5.35 MY: Ocean Drilling Program Site 625 northeast Gulf of Mexico. *Paleoceanography*, *5*(4), 507–529. https://doi.org/10.1029/pa005i004p00507

Kennett, J. P., & Von der Borch, C. C. (1986). Southwest Pacific paleoceanography. *Initial Report DSDP*, *90*, 1493–1515.

Mortimer, N., & Parkinson, D. (1996). Hikurangi Plateau: A Cretaceous large igneous province in the southwest Pacific Ocean. *Journal of Geophysical Research*, *101*(B1), 687–696. https://doi.org/10.1029/95jb03037

Wood, R. A., Andrews, P. B., Herzer, R. H., & Cook, R. A. (1989). *Cretaceous and Cenozoic geology of the Chatham Rise region, South Island, New Zealand*. New Zealand Geological Survey.